J. Fluid Mech. (2013), *vol.* 715, *pp.* 597–641. © Cambridge University Press 2013
doi:10.1017/jfm.2012.537

Minimum power consumption for drag reduction on a circular cylinder by tangential surface motion

Ratnesh K. Shukla† **and Jaywant H. Arakeri**

Department of Mechanical Engineering, Indian Institute of Science, Bangalore 560012, India

(Received 14 March 2012; revised 12 September 2012; accepted 26 October 2012)

We investigate the effect of a prescribed tangential velocity on the drag force on a circular cylinder in a spanwise uniform cross flow. Using a combination of theoretical and numerical techniques we make an attempt at determining the optimal tangential velocity profiles which will reduce the drag force acting on the cylindrical body while minimizing the net power consumption characterized through a non-dimensional power loss coefficient (C_{PL}). A striking conclusion of our analysis is that the tangential velocity associated with the potential flow, which completely suppresses the drag force, is not optimal for both small and large, but finite Reynolds number. When inertial effects are negligible ($Re \ll 1$), theoretical analysis based on two-dimensional Oseen equations gives us the optimal tangential velocity profile which leads to energetically efficient drag reduction. Furthermore, in the limit of zero Reynolds number ($Re \to 0$), minimum power loss is achieved for a tangential velocity profile corresponding to a shear-free perfect slip boundary. At finite Re, results from numerical simulations indicate that perfect slip is not optimum and a further reduction in drag can be achieved for reduced power consumption. A gradual increase in the strength of a tangential velocity which involves only the first reflectionally symmetric mode leads to a monotonic reduction in drag and eventual thrust production. Simulations reveal the existence of an optimal strength for which the power consumption attains a minima. At a Reynolds number of 100, minimum value of the power loss coefficient ($C_{PL} = 0.37$) is obtained when the maximum in tangential surface velocity is about one and a half times the free stream uniform velocity corresponding to a percentage drag reduction of approximately 77 %; $C_{PL} = 0.42$ and 0.50 for perfect slip and potential flow cases, respectively. Our results suggest that potential flow tangential velocity enables energetically efficient propulsion at all Reynolds numbers but optimal drag reduction only for $Re \to \infty$. The two-dimensional strategy of reducing drag while minimizing net power consumption is shown to be effective in three dimensions via numerical simulation of flow past an infinite circular cylinder at a Reynolds number of 300. Finally a strategy of reducing drag, suitable for practical implementation and amenable to experimental testing, through piecewise constant tangential velocities distributed along the cylinder periphery is proposed and analysed.

Key words: drag reduction, flow control, propulsion

† Email address for correspondence: ratnesh@mecheng.iisc.ernet.in

https://doi.org/10.1017/jfm.2012.537 Published online by Cambridge University Press

1. Introduction

Drag reduction is one of the most sought after goals in the studies on flow control over bluff bodies. Recent advances in the experimental techniques and computational resources have led to a surge in experimental, theoretical and computational investigations on drag reduction for flow past bluff bodies. A variety of active, passive and feedback flow control strategies ranging from the traditional strategies which employ preferential blowing and suction to more sophisticated strategies involving use of plasma actuators, synthetic jets, etc., have been proposed. The series of reviews contained in a recent theme issue on flow control approaches to drag reduction (Leschziner, Choi & Choi 2011) highlight the new methodologies along with their potential for impact and future challenges. From the viewpoint of practical implementation (Spalart & McLean 2011) emphasis has been placed on the importance of investigating not only the effective drag but also the net power consumed in countering the effective drag and in reducing it from its base value. A given control strategy can be deemed successful only if the power consumed in controlling the flow is less than the power savings that result from a reduction in drag.

For a given flow control strategy, knowledge of the optimal control parameters which reduce drag while minimizing the net power consumption is of utmost importance. In addition to setting a limit on performance, such an optimal configuration also serves as a benchmark to evaluate the merit of others (Choi, Jeon & Kim 2008). Beyond academic interest, knowledge of the optimal configuration has practical benefits. If simple enough it can be directly tested and implemented in an experiment. Even otherwise, simpler strategies could be devised which mimic this optimal configuration to achieve high performance. Such optimal energy minimizing solutions can be employed in cost function evaluation in feedback control methods for achieving better flow control authority and drag reduction. In their blowing-and suction-based control for flow over a sphere Jeon & Choi (2005) found that a cost function that minimizes the difference between surface pressures obtained from potential flow and the base flow gave higher drag reduction than a cost function based on the drag itself. The motivation here was that potential flow past a sphere gives zero drag independent of the Reynolds number.

Determining such optimal parameters for a control strategy based on a prescribed tangential surface velocity and investigating its effectiveness as a function of Reynolds number for flow past a circular cylinder, a representative bluff body flow problem, is our primary objective in this paper. The reasons behind the choice of a prescribed unidirectional surface motion as a means of achieving flow control for drag reduction are its simplicity, generality and its connection with the potential flow. Flow separation is the primary reason for the large drag force acting on a bluff body. A judicious choice of tangential surface velocity inhibits boundary layer growth by reducing the relative motion between wall and the free stream and depending on its strength relative to the free stream velocity delays or prevents its separation by injecting momentum into the existing boundary layer (Modi 1997). In addition, it is possible to analyse the general cases of drag reduction, self-propulsion and thrust production by varying the strength of the tangential surface velocity relative to the free stream velocity.

Potential flow can be viewed as the simplest example of an attempt at achieving flow control past a bluff body, where the tangential surface velocity is prescribed in a way that ensures that the entire flow remains irrotational. The velocity and pressure fields associated with the potential flow satisfy the incompressible Navier–Stokes equations and the no slip boundary condition corresponding to a no-through-flow

https://doi.org/10.1017/jfm.2012.537 Published online by Cambridge University Press

cylinder surface which moves with an appropriate prescribed tangential surface velocity. In general this does not necessarily imply that the flow is inviscid (Joseph, Funada & Wang 2007) and the finite viscous dissipation associated with the potential flow is balanced by the work that needs to be done against the viscous stresses acting on the surface of the bluff body. The drag reduction achieved in a potential flow is remarkable; a typical bluff body, for example a cylinder, does not experience any drag force in potential flow. The absence of vorticity in a potential flow seems to suggest that frictional losses are kept to a minimum and a maximum drag reduction is achieved while the disturbance kinetic energy resulting from the presence of the bluff body is minimized (Kelvin's theorem). These desirable characteristics of the potential flow have motivated a recent study on frictionless propulsion of elongated swimmers (Leshansky *et al.* 2007) at low Reynolds number. However, an analysis of whether or not potential flow represents the optimal way of achieving drag reduction does not appear to have been done in the literature to the best of the authors' knowledge.

The idea of utilizing moving walls to delay separation and reduce drag is not new. Use of a rotating cylinder at the leading edge or inside an aerofoil for increasing the lift coefficient has been mentioned in Prandtl & Tietjens (1957). Rotating cylinders placed on the leading edge along with supporting cylinders at the trailing edge and upper and lower surfaces could reduce drag and increase lift and stall angle. A comprehensive review of these earlier studies is summarized in Modi (1997) along with the demonstration of remarkable decrease in the drag coefficients through application of cylindrical tip rollers at the leading edge of an aerofoil and the sharp edges of a flat plate, D-section and triangular and square prisms. More recently Beaudoin *et al.* (2006) demonstrated their open- and closed-loop control of separation and achieved drag reduction by adaptively controlling the rotation rate of a circular cylinder placed at the edge of a backward facing step.

Tangential surface velocity can be realized by integrating rotating cylinders with bluff bodies and using them as tangential belt actuators in order to delay separation and reduce drag. Replacing a fixed wall with a passive belt which moves under the action of shear stress was found to lead to a drag reduction of 9 % (Bechert, Hage & Brusek 1996). An extension of this idea to flow past a circular cylinder was considered in the computational study of Choi & Choi (2000). It was shown that presence of tangential belt actuators in a region close to the separation points of the original cylinder delayed separation and led to a decrease in form and skin-friction drags. However, the energetic efficiency of the control input was not considered in this work. Subsequently Milano & Koumoutsakos (2002) considered optimization of a series of 16 segments of tangential belt actuators that were distributed over a circular cylinder through a genetic-algorithm-based computational study. The cost function chosen in their study minimized drag by seeking the optimal strengths of the tangential belt actuators and the energetic efficiency of the control was not considered. A maximum drag reduction of $\sim$50 % was obtained through an optimal distribution of the strength of the tangential belt actuators at a Reynolds number of 500. A fully three-dimensional optimization was attempted by including the possibility of spanwise variations through an extension of optimal two-dimensional tangential velocity profiles in Poncet *et al.* (2008). For a fixed kinetic energy of tangential belt motion a drag reduction of 33 % was obtained at Reynolds number of 300. However, the overall efficiency of this optimization was not evaluated on the basis of net power consumption in either of these references. Note that the tangential belt kinetic energy represents only a portion of the net power consumed and at high Reynolds numbers the contribution from vorticity becomes increasingly important (see § 4).

https://doi.org/10.1017/jfm.2012.537 Published online by Cambridge University Press

Tailored superhydrophobic surfaces (Rothstein 2010) have also emerged as a promising alternative for passive drag reduction and can be viewed as a member of the larger set of surface-tangential-velocity-based actuation, since a suitable choice of surface tangential velocity could lead to a vanishing tangential wall shear stress. The presence of alternating bands of finite slip and no-slip led to drag reductions of 8 and 27 % at Reynolds numbers of 300 and 3900, respectively, in You & Moin (2007). Legendre, Lauga & Magnaudet (2009) investigated the effect of slip on the wake, vortex shedding, drag and lift coefficients and vorticity intensity through two-dimensional numerical simulations of flow past a circular cylinder. The effect of slip on vortex shedding dynamics was studied experimentally by Muralidhar *et al.* (2011).

Although not directly related to the current investigation, drag reduction through transient oscillatory-rotation-based surface motion has received a lot of attention. Oscillatory rotation of a circular cylinder placed in a uniform cross flow was shown to reduce drag by as much as 80 % at a Reynolds number (based on diameter) of 1.5×10^4 (Tokumaru & Dimotakis 1991). The experimental work of Tokumaru & Dimotakis (1991) inspired several computational and experimental studies on rotary-oscillation-based flow control and drag reduction for flow past a circular cylinder (Shiels & Leonard 2001; Choi, Choi & Kang 2002; Poncet 2004; Thiria, Goujon-Durand & Wesfreid 2006). Selective application of oscillatory rotation on only an upstream portion of the circular cylinder was shown to generate a local thrust producing reverse von-Kármán street (Bergmann, Cordier & Brancher 2006) and a combination of rectilinear and rotational oscillation led to propulsion of a circular cylinder (Blackburn, Elston & Sheridan 1999; Nazarinia *et al.* 2009). The idea of employing two counter-rotating cylinders to produce a doublet-like structure (Prandtl & Tietjens 1957), which could propel in a predominantly irrotational flow, was explored from the perspectives of vortex-shedding suppression and propulsion (Yoon *et al.* 2007; Chan *et al.* 2011; Kumar, Gonzalez & Probst 2011).

The simplicity and ease with which oscillatory-rotation-based control strategy can be implemented has encouraged investigations aimed at determining the set of optimal forcing parameters for drag reduction. He *et al.* (2000) achieved up to 30–60 % drag reduction for flow past a two-dimensional circular cylinder undergoing oscillatory rotation for Reynolds number ranging from 200 to 1000. Adjoint-based optimization was used by Homescu, Navon & Li (2002) in order to suppress unsteady vortex shedding. Despite a decrease in the amplitude of fluctuations in the drag coefficient no appreciable decrease in the time-averaged drag coefficient was observed. Computationally efficient strategies based on proper orthogonal-decomposition-based reduced order models have been developed (Bergmann, Cordier & Brancher 2005; Bergmann & Cordier 2008) and used to determine optimal forcing parameters for rotary oscillation with the overall objective of drag reduction. Protas & Styczek (2002) considered overall energetic efficiency as their cost function to obtain optimal rotation rates of the circular cylinder. Unlike the remaining studies their active control led to drag reductions of 7 and 15 % at Reynolds numbers of 75 and 150 for high power-savings ratios (PSRs), a performance metric defined as the ratio of power saved through drag reduction to the power expended in rotary oscillation and discussed in more detail in § 2, of 122 and 51, respectively. However, their method was ineffective below a Reynolds number of 46 when vortex shedding is absent; the energetic efficiency of the optimal control deteriorated with an increase in Reynolds number due to the reduced control authority at high Reynolds number.

When the strength of the tangential surface velocity relative to the free stream is sufficiently high the drag acting on the bluff body vanishes and a self-propelling

https://doi.org/10.1017/jfm.2012.537 Published online by Cambridge University Press

configuration is obtained. The possibility of using continuous tangential surface rotation for propulsion of a toroidal swimmer at low Reynolds number was mentioned in the earlier works of Taylor (1952) and Purcell (1977). This so-called surface treadmilling mode of locomotion, in which a body propels as a result of tangential surface distortions which do not affect its shape, has been analysed in more detail recently (see Lauga & Powers 2009, for a review). The low energy-dissipation rates associated with streamlined microswimmers which employ this mode of locomotion imply that self-propulsion can be achieved with very high energetic efficiency (Leshansky *et al.* 2007). In the present context, one may view potential flow past a circular cylinder as a simple example involving tangential surface motion which results in a state of self-propulsion characterized by zero drag force, at any Reynolds number. The focus of this paper is on drag reduction but the generality of our treatment allows us to draw conclusions on the efficient propulsion of a circular cylinder which undergoes motion due to tangential surface velocity.

The paper is organized as follows. The set up of the problem under consideration is given in § 2. This includes identification of a non-dimensional power loss coefficient as an appropriate metric to assess energetic efficiency of the tangential surface velocity in reducing drag. The optimal tangential surface velocity which minimizes net power consumption while reducing the drag force exerted on a circular cylinder at low Reynolds number is identified in § 3 through a mathematical analysis based on linearization of the governing equations. In § 4 we first describe the numerical methodology adopted for investigations at a finite Reynolds number. Thereafter, results aimed at understanding the effect of first reflectionally symmetric mode of tangential surface velocity on the drag, power consumption and overall flow characteristics, at various Reynolds numbers, are presented and analysed. The energetic efficiency of tangential belt actuators in achieving drag reduction and propulsion through segments with constant tangential surface velocity is analysed in § 5 before the conclusions are drawn in § 6.

2. Problem statement

Consider the uniform two-dimensional incompressible flow of a viscous fluid past a stationary circular cylinder of diameter D as illustrated in figure 1. The free stream velocity field is given by $U_\infty \boldsymbol{i}$, where $\boldsymbol{i}$ is the unit vector in the x direction. The boundaries of the upper and lower halves of the cylinder undergo a prescribed reflectionally symmetric motion ($f(\pi + \theta) = -f(\theta) = f(2\pi - \theta)$) with a spanwise constant tangential velocity which is a function of only the location along the periphery of the cylinder. Pressure and viscous (normal and shear) stresses acting on the surface of the cylinder give rise to time-dependent lift and drag forces. The flow field is conveniently expressed in cylindrical coordinates (r, θ) with the cylinder surface given by $r = a$, where $a = 0.5D$ denotes the radius of the cylinder. The methodology used in determining the optimal tangential velocity profile $f(\theta)$, which reduces drag while minimizing the net power consumption, is described next.

2.1. *Governing equations*

The governing equations for the two-dimensional flow field depicted in figure 1 are the incompressible Navier–Stokes equations

$$\frac{\partial \boldsymbol{u}}{\partial t} + \boldsymbol{u} \cdot \boldsymbol{\nabla} \boldsymbol{u} = -\frac{1}{\rho} \boldsymbol{\nabla} p + \nu \nabla^2 \boldsymbol{u}, \quad \boldsymbol{\nabla} \cdot \boldsymbol{u} = 0, \tag{2.1}$$

https://doi.org/10.1017/jfm.2012.537 Published online by Cambridge University Press

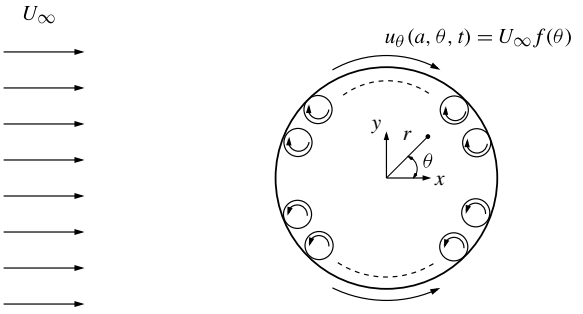


FIGURE 1. Schematic depicting the flow configuration.

along with the following no-slip boundary conditions:

$$u_r(a,\theta,t) = 0 \tag{2.2a}$$

$$u_\theta(a,\theta,t) = U_\infty f(\theta), \tag{2.2b}$$

where $\boldsymbol{u} = (u_r, u_\theta)$ denotes the velocity field in cylindrical polar coordinates along with pressure p, density of the fluid ρ and time t. Reynolds number based on the diameter of the cylinder $Re_D = U_\infty D/\nu$, where ν is the kinematic viscosity of the fluid. The pressure and viscous contributions to the forces acting on the cylinder can be expressed in terms of time-dependent non-dimensional drag and lift coefficients as follows:

$$C_D\boldsymbol{i} + C_L\boldsymbol{j} = (C_{D_p} + C_{D_f})\boldsymbol{i} + (C_{L_p} + C_{L_f})\boldsymbol{j}, \tag{2.3a}$$

$$C_{D_p} = -\frac{1}{\rho U_\infty^2}\int_0^{2\pi} p(a,\theta)\cos\theta\,\mathrm{d}\theta, \tag{2.3b}$$

$$C_{D_f} = \frac{1}{\rho U_\infty^2}\int_0^{2\pi} (\tau_{rr}(a,\theta)\cos\theta - \tau_{r\theta}(a,\theta)\sin\theta)\,\mathrm{d}\theta, \tag{2.3c}$$

$$C_{L_p} = -\frac{1}{\rho U_\infty^2}\int_0^{2\pi} p(a,\theta)\sin\theta\,\mathrm{d}\theta, \tag{2.3d}$$

$$C_{L_f} = \frac{1}{\rho U_\infty^2}\int_0^{2\pi} (\tau_{rr}(a,\theta)\sin\theta + \tau_{r\theta}(a,\theta)\cos\theta)\,\mathrm{d}\theta, \tag{2.3e}$$

where subscripts p and f denote pressure and friction, and τ_{rr} and $\tau_{r\theta}$ are the first two components of viscous stress tensor $\boldsymbol{\tau} = \mu(\boldsymbol{\nabla u} + (\boldsymbol{\nabla u})^{\mathrm{T}})$.

2.2. *Drag reduction with minimal power consumption*

The primary objective of the introduction of a non-zero tangential surface velocity is reduction of the drag force acting on the cylinder. However, to be useful, this strategy should lead to a reduction in not only drag but also the net power consumption. Net power consumption (P_T) is the sum of the rates at which work has to be done to counteract the drag force (P_D) acting on the body and to maintain a steady tangential velocity at the cylinder surface ($\dot{W}$). Note that this definition of the net power consumption is equivalent to the rate at which work must be done in order to tow the cylinder through an otherwise undisturbed fluid at a uniform speed U_∞ under the combined action of the prescribed surface tangential velocity and an external force

https://doi.org/10.1017/jfm.2012.537 Published online by Cambridge University Press

which counters the drag and lift forces. Thus, we have

$$P_T = P_D + \dot{W}, \tag{2.4a}$$

$$P_D = (C_D U_\infty)\, \rho U_\infty^2 a, \tag{2.4b}$$

$$\dot{W} = -a \int_0^{2\pi} \tau_{r\theta}(a, \theta) u_\theta(a, \theta)\, \mathrm{d}\theta. \tag{2.4c}$$

Relationships (2.4*a*), (2.4*b*) and (2.4*c*) can be derived by considering the basic definition of net power consumption in terms of the stress tensor for the flow configuration depicted in figure 1 in a reference frame that translates with a uniform velocity $-U_\infty \boldsymbol{i}$. The stress tensor is frame independent so that we can write $\tilde{\boldsymbol{\sigma}} = \boldsymbol{\sigma}$, where a tilde has been used to denote a quantity in the translating reference frame. Furthermore, velocity is given by $\tilde{\boldsymbol{u}} = \boldsymbol{u} - U_\infty \boldsymbol{i}$. In this reference frame the cylinder undergoes steady translation with a velocity $-U_\infty \boldsymbol{i}$ in an otherwise quiescent fluid and work is done in maintaining this steady translation. Therefore, total power consumption is given by

$$\tilde{P}_T = -\int_0^{2\pi} (\tilde{\boldsymbol{u}} \cdot \tilde{\boldsymbol{\sigma}} \cdot \boldsymbol{n}) a\, \mathrm{d}\theta = P_T, \tag{2.5}$$

where $\boldsymbol{n} = (\cos\theta, \sin\theta)$ denotes the normal to the circular cylinder. Rearranging (2.5) and expressing P_T in terms of the quantities defined in the original stationary reference frame depicted in figure 1 we obtain

$$P_T = U_\infty \boldsymbol{i} \cdot \int_0^{2\pi} (\boldsymbol{\sigma} \cdot \boldsymbol{n}) a\, \mathrm{d}\theta - \int_0^{2\pi} (\boldsymbol{u} \cdot \boldsymbol{\sigma} \cdot \boldsymbol{n}) a\, \mathrm{d}\theta. \tag{2.6}$$

Equation (2.6) can be simplified further by noting that the first integral that appears on the right-hand side is the total force exerted on the cylinder ($\rho U_\infty^2 a\{C_D \boldsymbol{i} + C_L \boldsymbol{j}\}$). In the case of uniform flow past a circular cylinder undergoing only tangential surface motions the following simplified expression

$$\dot{W} = -a \int_0^{2\pi} \boldsymbol{u} \cdot \boldsymbol{\sigma} \cdot \boldsymbol{n}\, \mathrm{d}\theta = -a \int_0^{2\pi} \tau_{r\theta}(a, \theta) u_\theta(a, \theta)\, \mathrm{d}\theta, \tag{2.7}$$

can be used to establish (2.4*a–c*).

The net power consumption P_T can be expressed in non-dimensional form through a power loss coefficient (Arakeri & Shukla 2012):

$$C_{PL} = C_D + \frac{\dot{W}}{\rho U_\infty^3 a}. \tag{2.8}$$

It should be noted that $C_{PL} = C_D$ whenever $\dot{W} = 0$, as in the case of a stationary boundary or perfect slip boundary with vanishing velocity or tangential wall shear stress, respectively. For a self-propelling cylinder $C_D = 0$ so that $C_{PL} = \dot{W}/(\rho U_\infty^3 a)$. Potential flow can be viewed as a special case of self-propulsion at any Reynolds number in that $C_D = 0$ and the flow field is an exact solution of the governing equations (2.1), (2.2*a*) and (2.2*b*), with $f(\theta) = -2\sin\theta$, for all Re_D. An explicit expression for the power loss coefficient corresponding to the potential flow can be obtained (see § 3):

$$C_{PL}^{pot} = \frac{16\pi}{Re_D}. \tag{2.9}$$

https://doi.org/10.1017/jfm.2012.537 Published online by Cambridge University Press

In the case of thrust generation, work done against wall shear stress dominates so that $\dot{W} > |\rho U_\infty^3 a C_D|$ and the power loss coefficient remains positive in spite of a negative drag coefficient.

For the flows considered in this work the mean time-averaged velocity and pressure fields depend only on the location in space and are independent of time so that conservation of energy implies that the net mean power consumption is balanced by the time-averaged viscous dissipation:

$$\rho U_\infty^3 a \overline{C}_{PL} = \mu \int_V \overline{\Phi}_v \, \mathrm{d}V \tag{2.10}$$

where $\Phi_v = (\boldsymbol{\tau}{:}\boldsymbol{\nabla u})/\mu$ is the dissipation function, V denotes the domain extending to ∞ and an overbar is used to denote time-averaged quantities.

At high Re_D an analysis of the energy budget for a control volume enclosing the circular cylinder can be used to show that the mean power consumption is balanced by the time-averaged viscous dissipation within the control volume and the mean rate at which kinetic energy is left behind in the wake of the cylinder (Arakeri & Shukla 2012):

$$\overline{\dot{W}} + \overline{P_D} = \mu \int_\Omega \overline{\Phi}_v \, \mathrm{d}V + \int_{\partial\Omega} \frac{1}{2} \rho \overline{u} \left(\| U_\infty \boldsymbol{i} - \overline{\boldsymbol{u}} \|^2 \right) \mathrm{d}A, \tag{2.11}$$

where Ω represents the control volume and the boundaries of the control volume $\partial\Omega$ are located sufficiently far downstream so that the pressure contribution to the total work may be neglected. The above expression (2.11) is an extension of the analysis presented in Prandtl & Tietjens (1957) where contribution from viscous dissipation was neglected.

The effectiveness of the tangential surface velocity in reducing drag needs to be evaluated against the flow corresponding to a stationary boundary for which $f(\theta) = 0$ using a performance metric. The performance metric should give a measure of the energetic efficiency and allow for an objective comparison between the various flow configurations which may result from a prescribed tangential surface velocity. In general, these include active drag reduction ($C_D > 0$), self-propulsion ($C_D = 0$) and thrust generation ($C_D < 0$).

In the past, the PSR defined as

$$\mathrm{PSR} = \frac{\overline{P}_D^0 - \overline{P}_D}{\overline{\dot{W}}}, \tag{2.12}$$

has been used extensively (Shiels & Leonard 2001; Protas & Styczek 2002; Bergmann & Cordier 2008) to characterize the effectiveness of an oscillatory-rotation-based control strategy in reducing drag on a circular cylinder. In the expression given by (2.12) $\overline{P}_D^0$ denotes the time-averaged work done against the drag force for a stationary cylinder, whereas $\overline{P}_D$ and $\overline{\dot{W}}$ denote the time-averaged work done against drag and in providing oscillatory rotation to the circular cylinder, respectively. The above definition of PSR is quite general and is applicable to the present case of a cylinder with a prescribed tangential velocity.

However, it is important to note that in the present context of a location-dependent tangential surface velocity, $\overline{\dot{W}}$ can become zero or even negative so that the power savings ratio can no longer be used as a metric of performance. The simplest of these cases arises when the prescribed surface velocity is such that the right-hand

https://doi.org/10.1017/jfm.2012.537 Published online by Cambridge University Press

side in (2.4*c*) becomes identically equal to zero (perfect slip for example). A similar situation arises in the familiar impulsively started uniform flow past a circular cylinder whose boundaries are unconstrained and detached from the rest of the body. One can imagine that the cylinder boundary is made up of closely spaced infinitesimally small cylindrical rollers (see figure 1) which are simply hinged to the primary cylinder and are free to rotate. In this hypothetical situation the shear stresses generated at the beginning of the impulsive start will lead to a differential but reflectionally symmetric rotation of each of the individual rollers placed along the periphery so that $\dot{W}$ is negative. Additional justification for this argument comes from the fact that the negligible amount of power $\dot{W}$ involved in rotating the cylinders at the leading and trailing edges of the aerofoil for moving surface boundary layer control has been mentioned as one of its strengths (Modi 1997).

In view of the above discussion we choose time-averaged power loss coefficient $\overline{C}_{PL}$ as a measure of the energetic efficiency. Since it represents the total non-dimensional time-averaged viscous dissipation in the flow field, $\overline{C}_{PL}$ is always positive and can be universally applied to drag reduction, propulsion and thrust generation cases. It is also closely related to the hydrodynamic efficiency for propulsion proposed by Lighthill (1952) and subsequently used in several later studies to assess propulsive efficiency of swimming bodies at low Reynolds numbers (Lauga & Powers 2009):

$$\eta_H = \frac{\overline{P}_T}{\overline{P}_T^0} = \frac{\overline{C}_{PL}}{\overline{C}_{PL}^0}. \tag{2.13}$$

In the present work we are primarily concerned with the percentage drag reduction and $\overline{C}_{PL}$ would give a measure of the energy required to achieve this. In general, the power loss coefficient can be interpreted as a measure of loss of energy; propulsive efficiency of thrusters and performance of wind turbines are directly related to the power loss coefficient (Arakeri & Shukla 2012).

Power loss coefficient has been used previously to analyse the effect of rotation rate on the power requirement in the study of flow past a single (Mittal & Kumar 2003) and two counter-rotating cylinders (Chan *et al.* 2011). Despite its generality and simplicity most studies on drag reduction do not seem to have evaluated the power loss coefficient. We consider finding $f(\theta)$ which minimizes C_{PL}. To accomplish this we first consider an expansion of $f(\theta)$ into its Fourier series:

$$f(\theta) = -\sum_{n=1}^{\infty} \alpha_n \sin(n\theta). \tag{2.14}$$

The problem thus reduces to determining the coefficients α_n such that the power loss coefficient C_{PL} is a minimum. In the next section we consider minimizing C_{PL} when the fluid is highly viscous so that $Re_D \ll 1$. Under this assumption the analysis becomes analytically tractable due to linearity of the governing equations which allows us to obtain an exact solution to the optimal flow field corresponding to minimum C_{PL}. Note that in expanding f as a Fourier sine series in (2.14) we have only assumed f to be an odd function ($f(\theta) = -f(-\theta)$). For a reflectionally symmetric tangential surface velocity f satisfies $f(\pi + \theta) = -f(\theta)$ in addition to $f(\theta) = -f(-\theta)$ so that the coefficients with even subscript in (2.14) are identically equal to zero ($\alpha_{2n} = 0, n = 1, 2, 3, \ldots$). The analysis presented in § 3 only requires $f(\theta) = -f(-\theta)$ and applies to more general tangential surface velocity profiles that may not be reflectionally symmetric. Therefore, we have retained the general expansion in (2.14) for the theoretical analysis detailed in the next section.

https://doi.org/10.1017/jfm.2012.537 Published online by Cambridge University Press

3. Flow past a circular cylinder with negligible inertia

We first consider determining the optimal coefficients $\alpha_n, n = 1, 2, 3, \ldots$ when $Re_D \ll 1$ so that the inertial effects are negligibly small except at distances very far away from the cylinder. Under this assumption Oseen equations, obtained by retaining only the zeroth-order term in the matched asymptotic expansion of the solution to Navier–Stokes equations, can be used to determine an approximation to the flow field in two dimensions. Note that there exist no solutions to two-dimensional Stokes equations which simultaneously satisfy far field and no-slip boundary conditions at the cylinder surface (Stokes paradox, cf. Batchelor 1967). A comprehensive overview of the analytical techniques available for estimating drag on a circular cylinder and sphere in the low-Reynolds-number regime, along with the application of renormalization-group theory, has been given in Veysey & Goldenfeld (2007). Here we take the general solution to the Oseen equations, which satisfy the no-normal flow boundary condition (2.2*a*), given by the following expression (Tomotika & Aoi 1950) for the stream function in cylindrical coordinates as the starting point of our analysis

$$\psi = U_\infty \left(r - \frac{a^2}{r}\right) \sin\theta + \frac{U_\infty}{4} \sum_{n=1}^{\infty} \sum_{m=0}^{\infty} \mathrm{B}_m \times \left\{ \left(\frac{a}{r}\right)^{n+1} \Phi_{m,n}(ka) - \Phi_{m,n}(kr) \right\} \frac{r \sin n\theta}{n}, \tag{3.1}$$

where

$$\Phi_{m,n}(kr) = \{\mathrm{K}_{m+1}(kr) + \mathrm{K}_{m-1}(kr)\}\{\mathrm{I}_{m-n}(kr) + \mathrm{I}_{m+n}(kr)\} + \mathrm{K}_m(kr) \times \{\mathrm{I}_{m-n-1}(kr) + \mathrm{I}_{m-n+1}(kr) + \mathrm{I}_{m+n-1}(kr) + \mathrm{I}_{m+n+1}(kr)\}. \tag{3.2}$$

In the above expression (3.2), I_p and K_q denote modified Bessel functions of pth and qth order, respectively, and $4ka = Re_D$. The solution given by (3.1) involves an infinite number of undetermined constants which can only be found by introducing an appropriate approximation in the form of a truncation (Veysey & Goldenfeld 2007). In order to satisfy the boundary condition (2.2*b*) on the tangential surface velocity up to N harmonics it is necessary to keep at least $N - 1$ terms in the inner summation. Setting the remaining coefficients to zero is the simplest possible truncation which allows for an explicit analytical determination of the constants from the boundary condition on tangential surface velocity. As mentioned in Veysey & Goldenfeld (2007) this choice also minimizes the truncation in the series expansion for a stationary cylinder boundary. Therefore, we follow this standard procedure of truncating the infinite summation in m and retaining only the first $n - 1$ terms. Using this approximation we obtain the following expressions for the velocity field

$$u_r = U_\infty \left(1 - \frac{a^2}{r^2}\right) \cos\theta + \frac{U_\infty}{4} \sum_{n=1}^{\infty} \sum_{m=0}^{n-1} \mathrm{B}_m \cos n\theta \times \left\{ \left(\frac{a}{r}\right)^{n+1} \Phi_{m,n}(ka) - \Phi_{m,n}(kr) \right\} \tag{3.3a}$$

$$u_\theta = -U_\infty \left(1 + \frac{a^2}{r^2}\right) \sin\theta + \frac{U_\infty}{4} \sum_{n=1}^{\infty} \sum_{m=0}^{n-1} \mathrm{B}_m \left(\frac{\sin n\theta}{n}\right) \times \left\{ n\left(\frac{a}{r}\right)^{n+1} \Phi_{m,n}(ka) + \Phi_{m,n}(kr) + kr\Phi'_{m,n}(kr) \right\}, \tag{3.3b}$$

https://doi.org/10.1017/jfm.2012.537 Published online by Cambridge University Press

where $\Phi'_{m,n}(kr) = \mathrm{d}\Phi_{m,n}(kr)/\mathrm{d}(kr)$. Comparison of (2.2*b*), (2.14) and (3.3*b*) gives us the following for the coefficients B_n

$$\mathrm{B}_0 = \frac{4(2-\alpha_1)}{2\Phi_{0,1}(ka) + ka\Phi'_{0,1}(ka)} \tag{3.4a}$$

$$\mathrm{B}_{n-1} = \frac{-4n\alpha_n - \sum_{m=0}^{n-2} \mathrm{B}_m\{(n+1)\Phi_{m,n}(ka) + ka\Phi'_{m,n}(ka)\}}{(n+1)\Phi_{n-1,n}(ka) + ka\Phi'_{n-1,n}(ka)}, \quad n > 1. \tag{3.4b}$$

The following limiting expressions for the modified Bessel's functions (Abramowitz & Stegun 1968) when $ka \ll 1$ ($Re_D \ll 1$)

$$\mathrm{K}_0(ka) \sim -\left\{\gamma + \ln\left(\frac{ka}{2}\right)\right\}, \quad \mathrm{I}_0(ka) \sim 1 \tag{3.5}$$

$$\mathrm{K}_n(ka) \sim \frac{\Gamma(n)}{2}\left(\frac{ka}{2}\right)^{-n}, \quad \mathrm{I}_n(ka) \sim \frac{1}{\Gamma(n+1)}\left(\frac{ka}{2}\right)^{n}, \quad n > 1, \tag{3.6}$$

can be used to obtain

$$\Phi_{0,n}(ka) \sim \frac{2}{\Gamma(n+1)}\left(\frac{ka}{2}\right)^{n-1}\left[1 - n\left\{\gamma + \ln\left(\frac{ka}{2}\right)\right\}\right] \tag{3.7}$$

$$\Phi_{m,n}(ka) \sim \frac{n}{2}\frac{\Gamma(m)}{\Gamma(n-m+1)}\left(\frac{ka}{2}\right)^{n-2m-1}, \quad 1 \leqslant m \leqslant n-1, \tag{3.8}$$

where $\gamma \approx 0.577$ denotes Euler's constant. Using the expressions above, (3.4*a*) and (3.4*b*) can be simplified and rewritten as

$$\mathrm{B}_0 \sim \frac{2-\alpha_1}{\frac{1}{2} - \gamma - \ln\left(\frac{ka}{2}\right)} \tag{3.9}$$

$$\begin{aligned}\mathrm{B}_{n-1} \sim {} & -\frac{4\alpha_n}{\Gamma(n-1)}\left(\frac{ka}{2}\right)^{n-1} - \frac{2}{n\Gamma(n)\Gamma(n-1)} \\ & \times \left[1 - 2n\left\{\gamma + \ln\left(\frac{ka}{2}\right)\right\}\right]\left(\frac{ka}{2}\right)^{2(n-1)}\mathrm{B}_0 \\ & - \sum_{m=1}^{n-2}\left[\frac{\Gamma(m)}{\Gamma(n-1)\Gamma(n-m)}\right]\left(\frac{ka}{2}\right)^{2(n-m-1)}\mathrm{B}_m.\end{aligned} \tag{3.10}$$

Furthermore, each of the successive terms in the above expression are in increasing powers of ka and of diminishing importance when $ka \ll 1$. Retaining only the significant terms we obtain a further simplification of (3.4*b*):

$$\mathrm{B}_0 \sim \frac{2-\alpha_1}{\frac{1}{2} - \gamma - \ln\left(\frac{ka}{2}\right)}, \quad \mathrm{B}_{n-1} \sim -\frac{4\alpha_n}{\Gamma(n-1)}\left(\frac{ka}{2}\right)^{n-1} \quad \text{for } n \geqslant 2. \tag{3.11}$$

This result is not surprising since linearity of the Oseen equations implies mode independence so that only the modes contained in the expression for tangential

https://doi.org/10.1017/jfm.2012.537 Published online by Cambridge University Press

velocity at the boundary appear in the solution for the entire flow field. Note that the procedure described above does not compromise the accuracy of the solutions since a zeroth-order approximation (in ka) to the flow field is the best we can achieve by solving Oseen equations. Following similar arguments and retaining only the terms which are of same order in ka we have

$$\tau_{rr}(a,\theta) = \frac{4\mu U_\infty}{a}\cos\theta - \frac{\mu U_\infty}{2a}\sum_{n=1}^{\infty} \mathrm{B}_{n-1}\{(n+1)\Phi_{n-1,n}(ka) + ka\Phi'_{n-1,n}(ka)\}\cos n\theta \tag{3.12a}$$

$$\sim \frac{2\mu U_\infty}{a}\sum_{n=1}^{\infty} n\alpha_n \cos n\theta \tag{3.12b}$$

$$\tau_{r\theta}(a,\theta) = \frac{4\mu U_\infty}{a}\sin\theta + \frac{\mu U_\infty}{4a}\sum_{n=1}^{\infty} \mathrm{B}_{n-1}\{-(n+1)^2\,\Phi_{m,n}(ka) + ka\Phi'_{m,n}(ka) + k^2a^2\Phi''_{m,n}(ka)\}\frac{\sin n\theta}{n} \tag{3.13a}$$

$$\sim \frac{4\mu U_\infty \sin\theta}{a}\left(\frac{\left(1-\gamma-\ln\left(\frac{ka}{2}\right)\right)\alpha_1 - 1}{1-2\gamma-2\ln\left(\frac{ka}{2}\right)}\right) + \frac{2\mu U_\infty}{a}\sum_{n=2}^{\infty} n\alpha_n \sin n\theta. \tag{3.13b}$$

Finally an expression for pressure on the surface of cylinder is required for estimating drag and net power consumption. Pressure is determined through a straightforward integration of the θ component of the Navier–Stokes equations as

$$p(a,\theta) = p_\infty - \frac{1}{2}\rho u_\theta^2 - \frac{\mu U_\infty}{4r}\sum_{n=1}^{\infty} \mathrm{B}_{n-1}\{k^3a^3\Phi'''_{n-1,n}(ka) + 4k^2a^2\Phi''_{n-1,n}(ka) + ka(1-n^2)\Phi'_{n-1,n}(ka) + (n^2-1)\Phi_{n-1,n}(ka)\}\frac{\cos n\theta}{n^2}, \tag{3.14}$$

where only the leading order terms in ka have been retained and p_∞ denotes the far field pressure. Next, drag which depends only on the first harmonic is computed as

$$F_D = a\int_0^{2\pi} ((\tau_{rr}-p)\cos\theta - \tau_{r\theta}\sin\theta)\,\mathrm{d}\theta$$

$$= \pi\mu U_\infty(2-\alpha_1)\left\{\frac{k^3a^3\Phi'''_{0,1}(ka) + 3k^2a^2\Phi''_{0,1}(ka) - 3ka\Phi'_{0,1}(ka)}{ka\Phi'_{0,1}(ka) + 2\Phi_{0,1}(ka)}\right\} \tag{3.15a}$$

$$\sim \pi\mu U_\infty \frac{2(2-\alpha_1)}{\frac{1}{2}-\gamma-\ln\left(\frac{ka}{2}\right)}. \tag{3.15b}$$

https://doi.org/10.1017/jfm.2012.537 Published online by Cambridge University Press

The rate at which work is done to sustain the motion of the cylinder boundary is given by

$$\dot{W} = -a\int_0^{2\pi} \tau_{r\theta} u_\theta \, \mathrm{d}\theta$$

$$= \pi\mu U_\infty^2 \left\{ 4\alpha_1 + \sum_{n=1}^{\infty} \frac{\alpha_n \mathrm{B}_{n-1}}{4n} [k^2 a^2 \Phi''_{n-1,n}(ka) + ka\Phi'_{n-1,n}(ka) \right.$$

$$\left. - (n+1)^2 \, \Phi_{n-1,n}(ka)] \right\} \tag{3.16a}$$

$$\sim 4\pi\mu U_\infty^2 \left(\frac{\left(1 - \gamma - \ln\left(\frac{ka}{2}\right)\right)\alpha_1^2 - \alpha_1}{1 - 2\gamma - 2\ln\left(\frac{ka}{2}\right)} \right) + 2\pi\mu U_\infty^2 \sum_{n=2}^{\infty} n\alpha_n^2. \tag{3.16b}$$

Therefore, the power loss coefficient assumes the following form

$$C_{PL} = \frac{F_D U_\infty + \dot{W}}{\rho U_\infty^3 a} \sim \frac{4\pi}{Re_D} \left\{ \frac{(1 - \gamma - \ln(Re_D/8))\alpha_1^2 - 2\alpha_1 + 2}{\frac{1}{2} - \gamma - \ln(Re_D/8)} + \sum_{n=2}^{\infty} n\alpha_n^2 \right\}; \tag{3.17}$$

the drag coefficient

$$C_D \sim \frac{4\pi}{Re_D} \frac{2 - \alpha_1}{\frac{1}{2} - \gamma - \ln(Re_D/8)}. \tag{3.18}$$

Clearly power loss coefficient attains a minimum of

$$C_{PL}^{opt} \sim \frac{8\pi}{Re_D} \left\{ \frac{1}{1 - \gamma - \ln(Re_D/8)} \right\}, \tag{3.19}$$

when

$$\alpha_1^{opt} \sim \frac{1}{1 - \gamma - \ln(Re_D/8)}, \quad \alpha_n^{opt} = 0 \quad \text{for } n > 1. \tag{3.20}$$

It is easy to see that the above optimal tangential velocity at the cylinder surface renders tangential wall shear stress $\tau_w^t = \tau_{r,\theta}(a, \theta) = 0$. Therefore, the optimal flow configuration coincides with that of perfect slip in which the shear stress vanishes everywhere on the cylinder surface. In addition, only the first mode ($n = 1$) is useful from the perspective of drag reduction; the remaining higher modes ($n > 1$) lead to an increase in the power loss without affecting drag.

It may seem that a vanishing tangential shear stress corresponding to a perfect slip cylinder boundary will lead to early separation. However, the aforementioned result of minimum power loss corresponding to a perfect slip boundary is derived under the assumption of $Re_D \to 0$ and we do not expect flow separation to occur when inertial effects are negligibly small. At moderate and high Reynolds numbers vorticity accumulation in the wake of the cylinder indicates whether or not boundary layers separate and form a recirculating zone which ultimately results in higher drag (Leal 1989; Magnaudet & Eames 2000). Unlike a stationary boundary, a perfect slip

https://doi.org/10.1017/jfm.2012.537 Published online by Cambridge University Press

boundary produces vorticity which scales as $O(1)$ independent of Re_D. This combined with an increasingly effective transport of vorticity at higher Re_D leads to formation of boundary layers which remain attached and do not separate from the cylinder surface. Therefore, we do not expect boundary layer separation for a circular cylinder with perfect slip boundary even at high Reynolds numbers ($Re_D \gg 1$). This fact is supported by the computational results of Legendre *et al.* (2009) (and also by our own results presented in § 4) in that an unseparated wake is formed behind a circular cylinder with a perfect slip boundary for Re_D up to 1000 (see Legendre *et al.* 2009, figures 1 and 4).

Similar conclusions can be drawn from a theoretical analysis based on Stokes equations for two-dimensional axisymmetric flow past a sphere translating with a given velocity U_∞. A minimum net power consumption rate of $4\pi\mu a U_\infty^2$ is achieved when the sphere experiences a net drag of $4\pi\mu a U_\infty$ corresponding to zero tangential shear stress, where μ and a denote the viscosity of the fluid medium and the radius of the sphere, respectively. To the best of the authors' knowledge this is the first time this result has been stated for axisymmetric flow past a sphere. This result can be obtained by considering the general solution of Stokes equations in spherical coordinates (see Happel & Brenner 1965, §§4–23) and its derivation is much simpler than that for a circular cylinder. Whether or not the above conclusion can be generalized to other geometries is still an open question which will be addressed in the future. At moderate values of Re_D there is no reason to believe that this conclusion will hold and higher modes could contribute to drag and cause a reduction in input work and the net dissipation.

The asymptotic forms of the minimum power loss coefficient C_{PL}^{opt} and the corresponding α_1^{opt} given by (3.19) and (3.20), respectively, were derived in the strict limit $Re_D \to 0$. The theoretical analysis presented in this section is not restricted to $Re_D \to 0$ and useful information on the optimal tangential surface velocity and corresponding minimum power loss and drag coefficients can be obtained by considering the following general expressions

$$\frac{C_D(\alpha_1)Re_D}{4\pi} = (2-\alpha_1)\left(\frac{k^3a^3\Phi'''_{0,1}(ka) + 3k^2a^2\Phi''_{0,1}(ka) - 3ka\Phi'_{0,1}(ka)}{4\Phi_{0,1}(ka) + 2ka\Phi'_{0,1}(ka)}\right), \quad (3.21)$$

$$\frac{C_{PL}(\alpha_1)Re_D}{4\pi} = \frac{C_D(\alpha_1)Re_D}{4\pi} + 2\alpha_1 + \alpha_1(2-\alpha_1)\left(\frac{k^2a^2\Phi''_{0,1}(ka) + ka\Phi'_{0,1}(ka) - 4\Phi_{0,1}(ka)}{4\Phi_{0,1}(ka) + 2ka\Phi'_{0,1}(ka)}\right), \quad (3.22)$$

which remain valid even when $Re_D \sim O(1)$. Note that $C_D(0) = C_{PL}(0)$ for a stationary boundary, $C_D(\alpha_1^{PS}) = C_{PL}(\alpha_1^{PS})$ for a perfect slip boundary and $C_D^{opt} = C_D(\alpha_1^{opt})$, $C_{PL}^{opt} = C_{PL}(\alpha_1^{opt})$ for the optimal configuration, where

$$\alpha_1^{opt} = \frac{9ka\Phi'_{0,1}(ka) - k^2a^2\Phi''_{0,1}(ka) - k^3a^3\Phi'''_{0,1}(ka)}{2k^2a^2\Phi''_{0,1}(ka) + 2ka\Phi'_{0,1}(ka) - 8\Phi_{0,1}(ka)}, \quad (3.23)$$

$$\alpha_1^{PS} = \frac{6ka\Phi'_{0,1}(ka) + 2k^2a^2\Phi''_{0,1}(ka)}{k^2a^2\Phi''_{0,1}(ka) + ka\Phi'_{0,1}(ka) - 4\Phi_{0,1}(ka)}. \quad (3.24)$$

Figure 2(*a*) depicts the drag and power loss coefficients, given by (3.21) and (3.22), as a function of Reynolds number for three cases corresponding to perfect slip, stationary boundary and the optimal configuration ($u_w^t = u_\theta(a,\theta) = -\alpha_1^{opt} U_\infty \sin\theta$)

https://doi.org/10.1017/jfm.2012.537 Published online by Cambridge University Press

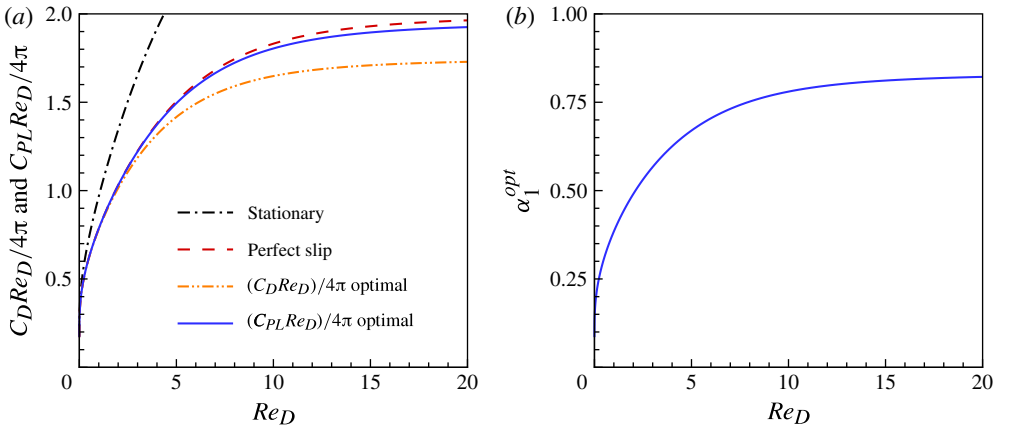


FIGURE 2. (Colour online) Drag and power loss coefficients (a) and α_1^{opt} (b) as a function of Re_D.

with minimum power loss coefficient. Note that for both the perfect slip and stationary cases $\dot{W} = 0$, thus $C_{PL} = C_D$. It is observed that at low Reynolds numbers the coefficients from the optimal and perfect slip cases coincide while at higher Re_D optimal α_1 leads to both a lower drag and lower power loss coefficient. In the limit $Re_D \to 0$ it can be easily shown that (3.24) assumes the asymptotic form given by the right-hand side of (3.20). Since both α_1^{opt} and α_1^{PS} converge to the same expression given by (3.20) we have $C_{PL}(\alpha_1^{opt}) = C_{PL}(\alpha_1^{PS}) \sim 8\pi/\{Re_D\,(1 - \gamma - \ln(Re_D/8))\}$ for $Re_D \to 0$. Therefore, power loss coefficients for the circular cylinder with a perfect slip boundary and the optimal tangential surface velocity are indistinguishable in the limit $Re_D \to 0$. For a finite non-zero Reynolds number α_1^{PS} and α^{opt} will no longer be equal so that power loss and drag coefficients corresponding to perfect slip and optimal configuration differ for $Re_D \sim O(1)$, with the differences increasing with increasing Re_D (see figure 2a).

Figure 2(a) clearly demonstrates that both the optimal and perfect slip are much more energetically efficient than the potential flow which has a power loss coefficient of $16\pi/Re_D$ ($C_{PL}Re_D/(4\pi) = 4$). These results are a bit unexpected because the optimal solution does not correspond to potential flow and a finite amount of vorticity is required to achieve the minimum power loss coefficient. A more detailed analysis is conducted in the next section where we highlight the root cause for this surprising result by relating the net power consumption to total vorticity and the tangential surface velocity. Figure 2(b) depicts the Reynolds number dependence of the optimal α_1 (α_1^{opt} from (3.23)) which minimizes power loss coefficient; α_1^{opt} is much lower than $\alpha_1 = 2$ for the potential flow.

4. Flow past a circular cylinder at finite Re_D

In this section we consider determining optimal coefficients α_n which minimize C_{PL} at a given finite Re_D. Owing to nonlinearity we no longer have mode independence and even though the drag coefficient C_D is determined by the first mode all the modes in (2.14) contribute to C_{PL} in a complex way so that C_{PL} can no longer be expressed in a simple quadratic form as in (3.17). Furthermore, the conclusion that higher modes simply lead to an increase in C_{PL} at low Re_D may not hold when inertial

https://doi.org/10.1017/jfm.2012.537 Published online by Cambridge University Press

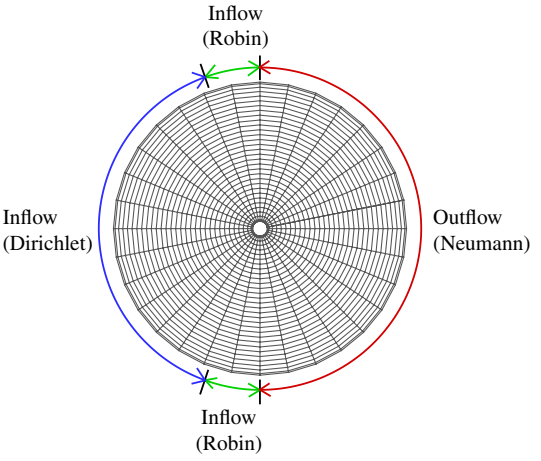


FIGURE 3. (Colour online) A representative computational domain and spatial discretization. Dirichlet, Neumann and Robin boundary conditions on the outer boundary of the computational domain are given by $\boldsymbol{u} = \boldsymbol{u}^{pot}$, $\partial_r \boldsymbol{u} = \partial_r \boldsymbol{u}^{pot}$ and $\boldsymbol{u} + \beta \partial_r \boldsymbol{u} = \boldsymbol{u}^{pot} + \beta \partial_r \boldsymbol{u}^{pot}$, respectively, where $\boldsymbol{u}^{pot}$ denotes the velocity field for a potential flow.

effects become increasingly dominant. Determining the full set of optimal coefficients as a function of Re_D, which in general could also be time dependent, is a daunting task and beyond the scope of the current work. Motivated by the results obtained in the previous section and the fact that for a potential flow, with $f(\theta) = -2\sin\theta$, the power loss coefficient decreases with increasing Re_D ($C_{PL}^{pot} = 16\pi/Re_D$) we conduct numerical simulations to analyse the effect of only the first mode, i.e. $f(\theta) = -\alpha_1 \sin\theta$. Unlike the case with $Re_D \ll 1$ the optimal solutions that we obtain may not necessarily correspond to a global minimum in C_{PL} and it is possible that a lower value of C_{PL} than that predicted could be achieved by employing a tangential velocity profile which involves higher modes. However, as we shall see in the following subsections despite this simplification we obtain flow configurations for which power loss coefficients achieved are significantly lower than not only the potential flow but also those with perfect slip on the cylinder surface.

The non-dimensionalized incompressible Navier–Stokes equations in the primitive variable formulation $(\boldsymbol{u}, p)$ are solved with a second-order semi-implicit projection method (Hugues & Randriamampianina 1998) which relies on Adams Bashforth and the backward differentiation formula (BDI) for temporal discretization of nonlinear convective and linear viscous terms, respectively. Spatial discretization is accomplished through a Fourier spectral method in the θ direction and a 10th-order compact scheme in the radial direction. Figure 3 shows a representative computational grid employed in the simulations. Non-uniform grid spacings are used in the radial direction in order to obtain stable discretizations using the 10th-order compact scheme both in the interior and at the boundaries of the computational domain (Shukla & Zhong 2005). A constant time step which ensures that the convective Courant–Friedrichs–Levy (CFL) stability criterion is satisfied all throughout the simulation is utilized for temporal discretization.

In order to minimize spurious reflections from the outflow boundary a Neumann boundary condition on the velocity fields is applied on the downstream region of the outer boundary (Mittal & Balachandar 1996) as depicted in figure 3. In addition it

https://doi.org/10.1017/jfm.2012.537 Published online by Cambridge University Press

is necessary to maintain control over the incoming flow through a Dirichlet boundary condition on the inflow boundary. However, a numerical solution computed from purely Dirichlet boundary condition on the inflow and Neumann boundary condition on the outflow will suffer from Gibb's oscillations that result from the singularities at the inflow–outflow junction ($\theta = \pi/2, 3\pi/2$) and are transmitted throughout the computational domain due to the global nature of a high-order compact scheme. One could consider a mixed Robin boundary condition on a portion of the inflow boundary that will ensure a smooth transition from the Dirichlet to Neumann boundary condition. However, this would be at the expense of a reduced control over the incoming flow resulting from a primarily Neumann boundary condition in a small region on the inflow boundary next to the inflow–outflow junction. Therefore, we have chosen the inflow and outflow boundary conditions described in figure 3, where the small factor β that varies smoothly from 0 at the inflow to 0.1 at the outflow offers some flexibility between these two extremes. A boundary condition of this form helps control numerical oscillations while maintaining a primarily Dirichlet boundary condition at the inflow boundary and was found to give accurate solutions for flow past circular and elliptic cylinders in two and three dimensions (Mittal & Balachandar 1996). For completeness further details of the numerical methodology and the results from test cases used for code verification are given in appendix A.

In order to analyse the effect of α_1 on C_{PL} and C_D at a given Re_D we first simulate a case corresponding to a stationary boundary with $\alpha_1 = 0$. An initial perturbation in the form of oscillatory rotation is imparted to the cylinder for the first few time steps in order to promote instabilities in the wake with the purpose of reducing computational expense. For all other non-zero α_1 simulations the long time solution computed for $\alpha_1 = 0$ is used as an initial condition. The computational parameters such as the extent of the outflow boundary, time step size, etc., are chosen according to stability and convergence requirements which depend on Re_D. In all of the test cases presented in this paper no appreciable change is observed when the results are compared with computations on a refined grid with a reduced time step.

4.1. *Simulation results*

Simulations are conducted for a range of Re_D from 1 to 300 for various values of the parameter α_1. In order to analyse the effect of α_1 on the overall flow we begin with the results of the simulation at $Re_D = 100$. In the following sections we use the phrase 'optimal' to denote the solution which is obtained by minimizing the power loss coefficient by varying α_1 in $u_w^t = -\alpha_1 U_\infty \sin\theta$ with the understanding that this may not necessarily correspond to a global minimum in C_{PL}.

4.1.1. *Flow characteristics at* $Re_D = 100$

Figure 4 depicts vorticity and streamfunction isocontours for different runs with varying α_1. We observe that with a gradual increase in α_1 the unsteady vortex shedding behind the cylinder is first diminished (figure 4*b,c*) and then completely suppressed for $\alpha_1 > 0.5$. The magnitude of vorticity close to the cylinder surface and that shed into the wake are also reduced along with the strength of the shear layer that separates from the cylinder surface. We also find that a standing eddy detached from the cylinder is formed when $\alpha_1 = 0.4$ (see figure 4*c*). Similar detached recirculating wake has been observed previously in the case of flow past ellipsoidal bubbles (e.g. Blanco & Magnaudet 1995). The most likely cause for the formation of this standing eddy in the present case is the existence of favourable conditions which result from a reduction in the magnitude of the surface vorticity accompanied by the efficient convection of

https://doi.org/10.1017/jfm.2012.537 Published online by Cambridge University Press

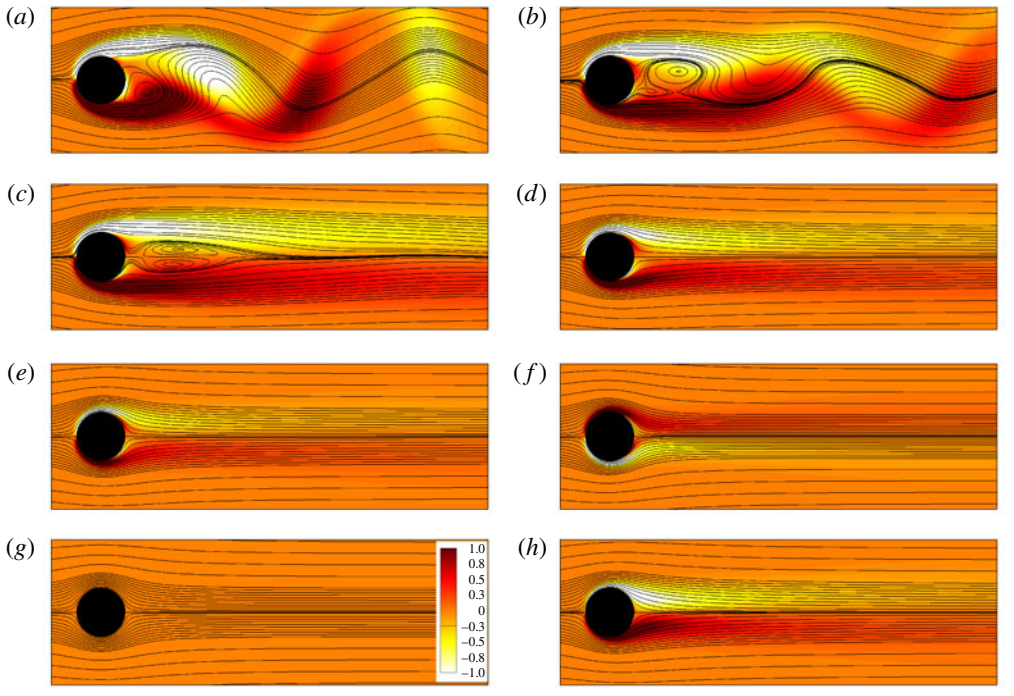


FIGURE 4. (Colour online) Effect of α_1 on the flow field at $Re_D = 100$ illustrated through vorticity isocontours and streamfunction: (*a*) stationary, $\alpha_1 = 0, \overline{C}_D = \overline{C}_{PL} = 1.344$; (*b*) $\alpha_1 = 0.3, \overline{C}_D = 0.993, \overline{C}_{PL} = 0.915$; (*c*) $\alpha_1 = 0.4, \overline{C}_D = 0.889, \overline{C}_{PL} = 0.796$; (*d*) $\alpha_1 = 1.0, C_D = 0.568, C_{PL} = 0.467$; (*e*) $\alpha_1 = 1.47$ (optimal), $C_D = 0.306, C_{PL} = 0.375$; (*f*) $\alpha_1 = 2.5, C_D = -0.303, C_{PL} = 0.888$; (*g*) potential flow, $\alpha_1 = 2, C_D = 0, C_{PL} = 0.503$; (*h*) perfect slip, $\tau_w^t = 0, C_D = C_{PL} = 0.417$.

the vorticity at high Re_D (Leal 1989; Magnaudet & Eames 2000). Of course, for potential flow ($\alpha_1 = 2$), vorticity vanishes identically and there is no wake.

At still higher values of α_1 the vorticity on the cylinder surface continues to decrease (figure 4*d,e*) before it undergoes a sign inversion when $\alpha_1 > 2$ (figure 4*f*). At a sufficiently high value of α_1 the tangential velocity on the cylinder surface reduces the maximum vorticity at the cylinder surface to an extent that separation is prevented. This is more clearly evident from figure 5(*a*) where an increase in α_1 leads to a reduction in the angle (measured with respect to downstream stagnation point) at which flow separates. It is also found (not shown here) that flow separation is completely prevented for $\alpha_1 > 1.8$. Figure 5(*b*) depicts the pressure coefficient:

$$C_p = \frac{2(p - p_\infty)}{\rho U_\infty^2}, \tag{4.1}$$

as a function of the location along the cylinder surface for various choices of the parameter α_1. With increase in α_1 pressure coefficient begins to recover to increasingly higher values at the rear stagnation point. This recovery is also evidenced in the drag coefficient which shows a monotonic decrease with increasing α_1 (figure 6*a*). Both viscous (C_{D_S}) and pressure (C_{D_P}) contributions to the net drag coefficient (C_D) show a higher rate of decline in the presence of vortex shedding, when $\alpha_1 < 0.5$.

https://doi.org/10.1017/jfm.2012.537 Published online by Cambridge University Press

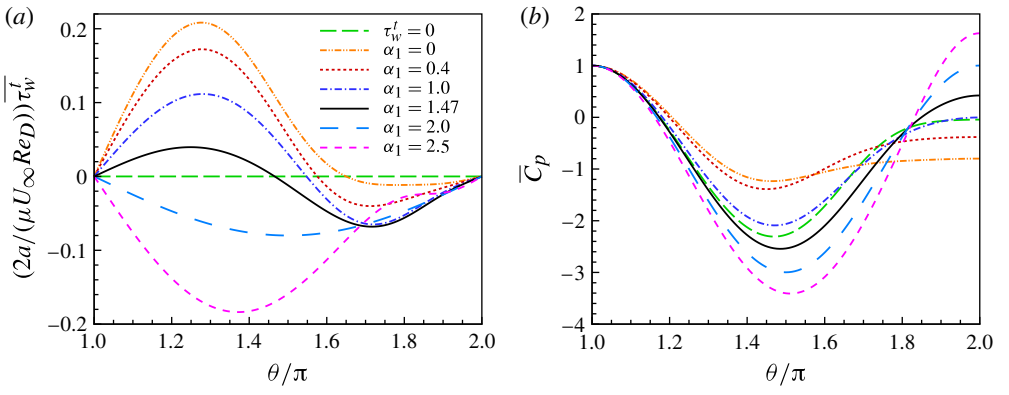


FIGURE 5. (Colour online) Mean tangential shear stress (*a*) and pressure coefficient (*b*) on the cylinder surface at $Re_D = 100$.

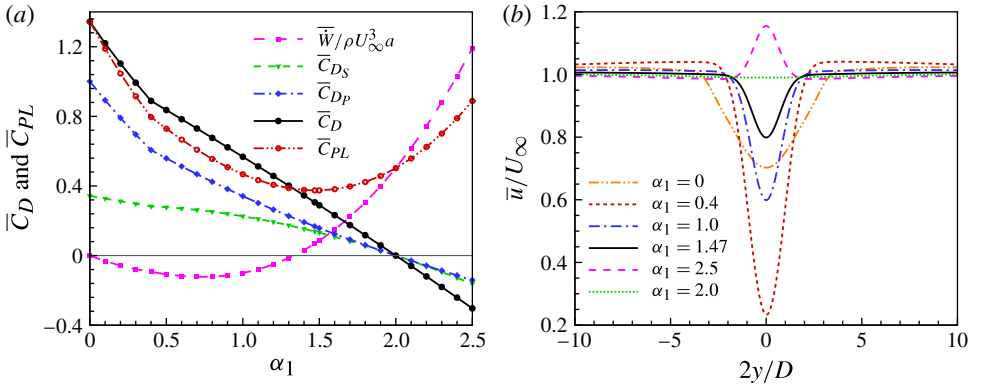


FIGURE 6. (Colour online) (*a*) Time-averaged drag and power loss coefficients as a function of α_1 at $Re_D = 100$. (*b*) Time-averaged streamwise velocity as a function of vertical location at $x = 5D$ for $Re_D = 100$.

The power loss coefficient also follows a similar trend for $\alpha_1 < 0.5$ except that the initial rate of decrease is higher than that of C_D owing to a negative $\overline{\dot{W}}$ corresponding to the tendency of the cylinder boundary to move along with the flow in a reflectionally symmetric manner. At still higher α_1 the power loss coefficient attains a minimum value of 0.375 when $\alpha_1 = 1.47$ with $C_D = 0.306$. Beyond this point the drag coefficient continues to decline until it reaches a value of zero for potential flow ($\alpha_1 = 2.0$). Increasing α_1 beyond 2 gives a thrust producing wake (figure 6*b*) and the cylinder experiences a net force in a direction opposite to the free stream ($C_D < 0$). The minimum value of power loss coefficient and the corresponding drag coefficient are both lower than a value of $C_{PL} = C_D = 0.417$ for a perfect slip boundary. These results are consistent with our analytical estimates presented in § 3 in that the minimum value of power loss coefficient achievable at a finite Re_D is less than the corresponding value for a perfect slip boundary.

In order to gain further insight into the effect of tangential velocity on net power consumption we present plots of the non-dimensional dissipation function $a^2\Phi_v/U_\infty^2$

https://doi.org/10.1017/jfm.2012.537 Published online by Cambridge University Press

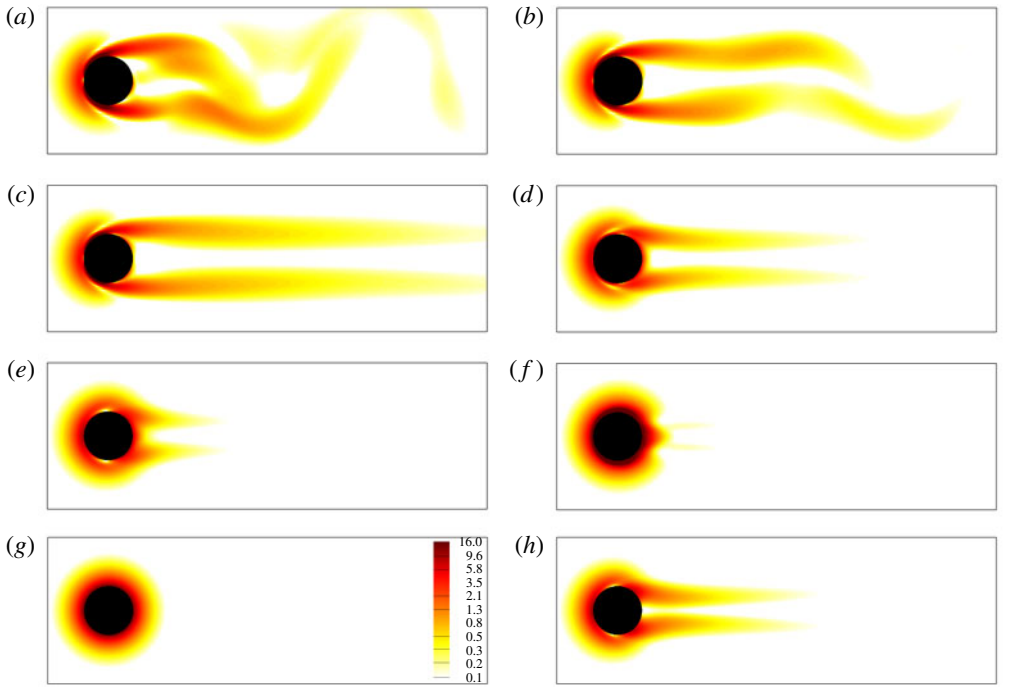


FIGURE 7. (Colour online) Effect of α_1 on the non-dimensional dissipation function $a^2\Phi_v/U_\infty^2$ at $Re_D = 100$: (*a*) stationary, $\alpha_1 = 0$; (*b*) $\alpha_1 = 0.3$; (*c*) $\alpha_1 = 0.4$; (*d*) $\alpha_1 = 1.0$; (*e*) $\alpha_1 = 1.47$ (optimal); (*f*) $\alpha_1 = 2.5$; (*g*) potential flow, $\alpha_1 = 2$; (*h*) perfect slip, $\tau_w^t = 0$.

in figure 7 for the various test cases considered in this section. The dissipation function attains a maximum on the cylinder surface and a significant amount of energy is dissipated not only close to the cylinder but also in the wake when $\alpha_1 \leqslant 1.0$ (figure 7*a–d*). As α_1 increases beyond this value the magnitude of dissipation function reduces in the vicinity of the cylinder and in the wake. For the potential flow (figure 7*g*) the dissipation function is radially symmetric ($a^2\Phi_v/U_\infty^2 = 16\,(a/r)^6$) and is confined to a small region surrounding the cylinder. A perfect slip cylinder boundary (figure 7*h*) leads to an energy loss which is lower than that of the potential flow but higher than that corresponding to the optimal configuration with $\alpha_1 = 1.47$ (figure 7*e*). For $\alpha_1 > 2$ (figure 7*f*) the dissipation function still remains localized to a narrow region surrounding the cylinder. However, the maximum value of the dissipation function rises with an increase in α_1 thereby leading to a high power loss coefficient.

4.1.2. *Drag and power loss coefficients as a function of* Re_D

From the results presented in the previous section it is clear that neither the potential flow nor the flow associated with a perfect slip boundary represent the power loss minimizing optimal flow configuration when inertial effects are important and a power loss coefficient which is lower than both is attainable. It is of interest to know how this result changes with Re_D and assess how the gain over potential flow and flow with a perfect slip boundary, that can be achieved by choosing an optimal α_1, scales with Re_D.

https://doi.org/10.1017/jfm.2012.537 Published online by Cambridge University Press

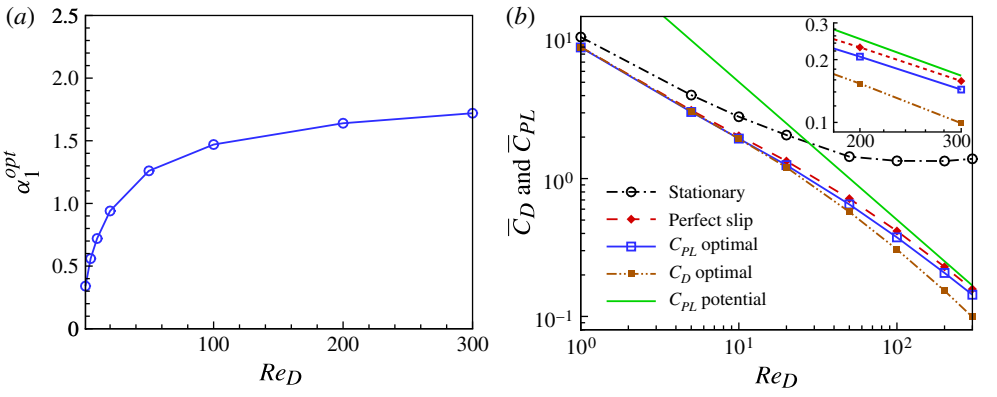


FIGURE 8. (Colour online) (*a*) Optimal α_1 (α_1^{opt}) which minimizes C_{PL} as a function of Re_D. (*b*) Drag and power loss coefficients as a function of Re_D for a stationary boundary, a perfect slip boundary, the optimal configuration and the potential flow.

In order to establish the Reynolds number dependence of the optimal α_1 which minimizes C_{PL} we perform a series of two-dimensional simulations for flows with varying α_1 for different choices of Re_D ranging from 1 to 300. Figure 8(*a*) shows the optimal α_1 which minimizes C_{PL} as a function of Re_D. Starting from a value of 0.34 at $Re_D = 1$, α_1^{opt} continues to increase with an increase in Re_D attaining a value of 1.72 for $Re_D = 300$. Our results seem to indicate that α_1^{opt} asymptotes to a value of 2 corresponding to the potential flow as $Re_D \to \infty$.

Figure 8(*b*) shows the drag and power loss coefficients as a function of Re_D. Note that the drag and power loss coefficients for a perfect slip boundary and a stationary boundary are equal ($C_D = C_{PL}$, if $\dot{W} = 0$). The differences between optimal and potential flow power loss coefficients are easily discernible at low Re_D. However, these differences continue to diminish with an increase in Re_D. Also noticeable is the fact that at low Re_D the power loss coefficients for the optimal configuration and the flow corresponding to a perfect slip boundary match one another and the difference between the two becomes significant only when inertial effects become important. When the Reynolds number is less than 50, the power loss coefficient for the flow with a stationary boundary decreases with increasing Re_D at a rate which is lower than those for the optimal configuration and the flow with a perfect slip boundary. The presence of unsteady vortex shedding beyond a critical $Re_D \approx 47$ leads to a change in this trend and the drag and, hence, the power loss coefficient for the stationary boundary shows a slight increase beyond $Re_D = 100$. In contrast, the power loss coefficients for the flow with a perfect slip boundary and optimal configuration decrease with increasing Reynolds number for all Re_D up to 300 and remain lower than that for a stationary boundary. As $Re_D \to \infty$, the power loss coefficient for the optimal configuration seems to converge asymptotically to a value of $16\pi/Re_D$ corresponding to the potential flow. The trends are very similar for the flow with a perfect slip boundary except that the power loss coefficient is always higher than that for the optimal configuration. The power loss coefficient for the potential flow remains higher than that for a stationary boundary when $Re_D \lessapprox 25$.

A summary of the drag and power loss coefficients for the stationary, perfect slip and optimal configuration at various Re_D is given in table 1. The low drag and power loss coefficients reveal the advantage of an optimal configuration over all of

https://doi.org/10.1017/jfm.2012.537 Published online by Cambridge University Press

https://doi.org/10.1017/jfm.2012.537 Published online by Cambridge University Press

Source	Re_D	$\overline{C}_D$			$\overline{C}_{PL}$	
		Stationary	Perfect slip	Optimal	Optimal	$C_D = 0$
Present	1	10.64	9.01	8.99	9.00	50.26
	5	4.04	3.13	3.05	3.07	10.05
	10	2.81	2.04	1.94	1.95	5.03
	20	2.07	1.34	1.21	1.25	2.51
	50	1.44	0.72	0.57	0.65	1.01
	100	1.34	0.42	0.31	0.37	0.50
	200	1.34^{2D}	0.23	0.15	0.21	0.25
	300	1.39^{2D}	0.16	0.10	0.14	0.17
			Optimal		Optimal	$C_D = 0$
Present (two segments)	100		0.58		0.68	1.21
Present (six segments)	100		0.42		0.47	0.74
Poncet *et al.* (2008)	300		0.862		—	
(Spanwise variations)	1000		0.65		—	
Milano & Koumoutsakos (2002) (16 piecewise constant segments)	500		0.7		—	
Shiels & Leonard (2001) (Sinusoidal oscillatory rotation)	3000		0.77		0.93	
	5000		0.73		0.86	
	8000		0.55		0.65	
	15 000		0.43		0.50	

TABLE 1. (Continued on next page)

https://doi.org/10.1017/jfm.2012.537 Published online by Cambridge University Press

Source	Re_D	$\overline{C}_D$	$\overline{C}_{PL}$
Protas & Styczek (2002)	75	1.14	1.14
(Oscillatory rotation)	150	1.02	1.02
Bergmann *et al.* (2005)	200	1.04	2.39
(Sinusoidal oscillatory rotation)			
Bergmann & Cordier (2008)	200	0.992	6.68
(Sinusoidal oscillatory rotation)			

TABLE 1. Comparison of drag and power loss coefficients. The first eight rows give the present results for drag and power loss coefficients for the flow with a stationary boundary, perfect slip boundary and the optimal configuration with $u_w^t = -\alpha_1^{opt} U_\infty \sin\theta$. The power loss coefficient for a self-propelling configuration corresponding to $C_D = 0$ is tabulated in the last column. Next two rows summarize the minimum power loss coefficients, corresponding drag coefficients and the power loss coefficient for a self-propelling cylinder when two and six segments with piecewise constant tangential velocity are used along the periphery. Results from other investigations on reduction of drag on a circular cylinder using tangential surface velocity are tabulated in the remaining rows. The power loss coefficients in the studies of Poncet *et al.* (2008) and Milano & Koumoutsakos (2002) could not be estimated and are therefore not given in the table. Results from test runs which resulted in a minimum power loss coefficient for a given Reynolds number in the study of Shiels & Leonard (2001) are presented for $Re_D \geqslant 3000$. Tables summarizing power savings ratio and relative drag reduction for oscillatory rotation based control of flow over a circular cylinder can be found in Bergmann & Cordier (2008) and Bergmann *et al.* (2005).

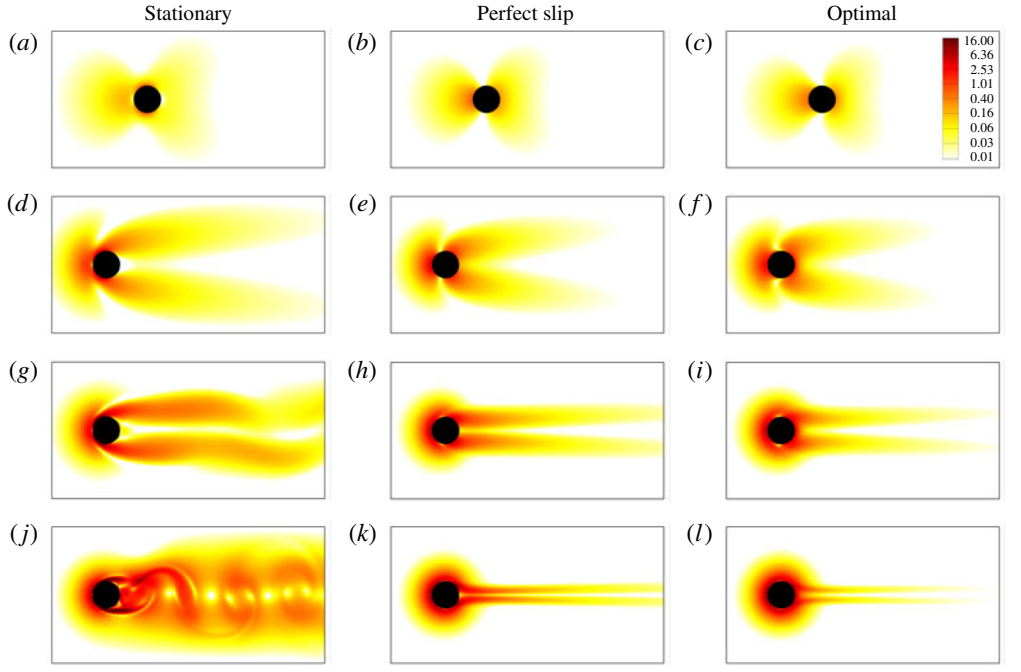


FIGURE 9. (Colour online) Effect of Re_D on the non-dimensional dissipation function for the stationary, perfect slip and optimal flow configuration with $u_w^t = -\alpha_1^{opt} U_\infty \sin\theta$. Dissipation function for potential flow is shown in figure 7(*g*): (*a*) stationary, $Re_D = 1$, $C_D = C_{PL} = 10.64$; (*b*) perfect slip, $Re_D = 1$, $C_D = C_{PL} = 9.01$; (*c*) $\alpha_1 = 0.34$, $Re_D = 1$, $C_D = 8.99$, $C_{PL} = 9.00$; (*d*) stationary, $Re_D = 10$, $C_D = C_{PL} = 2.81$; (*e*) perfect slip, $Re_D = 10$, $C_D = C_{PL} = 2.04$; (*f*) $\alpha_1 = 0.72$, $Re_D = 10$, $C_D = 1.94$, $C_{PL} = 1.95$; (*g*) stationary, $Re_D = 50$, $\overline{C}_D = \overline{C}_{PL} = 1.44$; (*h*) perfect slip, $Re_D = 50$, $C_D = C_{PL} = 0.72$; (*i*) $\alpha_1 = 1.26$, $Re_D = 50$, $C_D = 0.57$, $C_{PL} = 0.65$; (*j*) stationary, $Re_D = 300$, $\overline{C}_D = \overline{C}_{PL} = 1.39$; (*k*) perfect slip, $Re_D = 300$, $C_D = C_{PL} = 0.16$; (*l*) $\alpha_1 = 1.72$, $Re_D = 300$, $C_D = 0.1$, $C_{PL} = 0.14$.

the remaining, stationary, perfect slip and potential flow. Overall, among the three possible strategies explored in this section, the optimal configuration gives maximum drag reduction for least power consumption at all Reynolds numbers.

Since our principal interest is in the power loss coefficient it is useful to investigate how the tangential surface velocity effects net energy dissipation at different Re_D. Figure 9 depicts a comparison of the non-dimensional dissipation function for the stationary, perfect slip and the optimal configurations at various Re_D. At $Re_D = 1$ the three are comparable with each other despite some minor differences between the stationary and the other two cases. The differences become more prominent with an increase in Re_D. At the highest $Re_D = 300$ considered in this work, the dissipation function attains maximum values on the surface of the cylinder and in the shear layers that separate from it. The extent of the dissipation function in the wake region is also enhanced significantly. Compared with the flow with a perfect slip boundary, the optimal configuration leads to a dissipation function which has a compact support and does not extend far downstream into the wake region (shown as yellow contours in the online version of figure 9). Furthermore, regions of high dissipation (depicted by dark red regions in the online version of figure 9) are more closely packed in the vicinity of the cylinder in the case of optimal configuration.

https://doi.org/10.1017/jfm.2012.537 Published online by Cambridge University Press

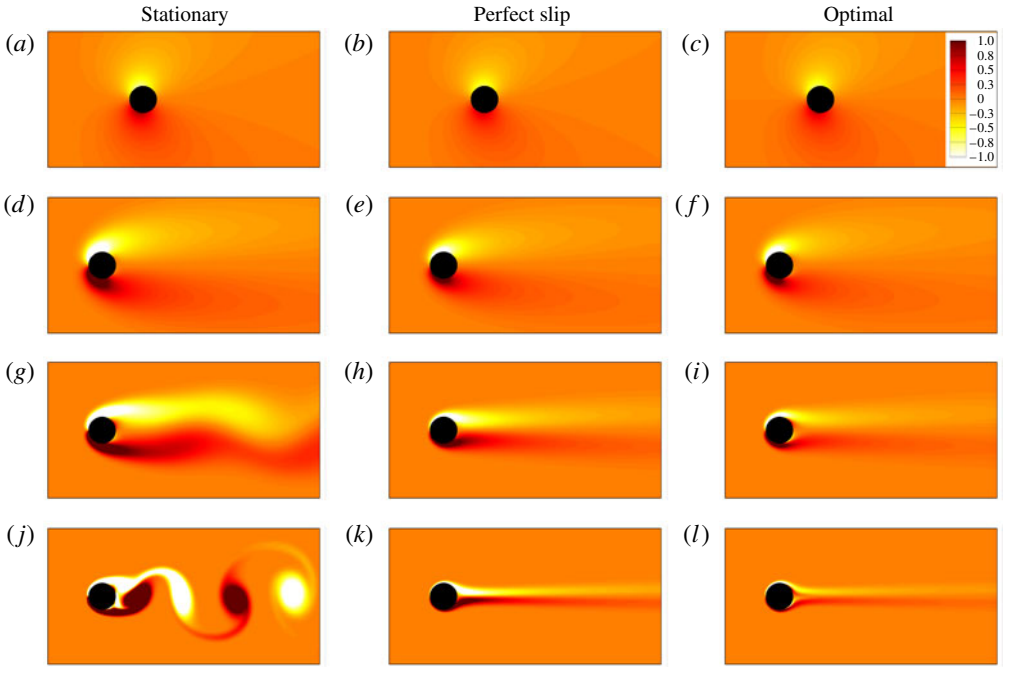


FIGURE 10. (Colour online) Effect of Re_D on the vorticity field for the stationary, perfect slip and optimal flow configuration with $u_w^t = -\alpha_1^{opt} U_\infty \sin\theta$: (*a*) stationary, $Re_D = 1$; (*b*) perfect slip, $Re_D = 1$; (*c*) $\alpha_1 = 0.34$, $Re_D = 1$; (*d*) stationary, $Re_D = 10$; (*e*) perfect slip, $Re_D = 10$; (*f*) $\alpha_1 = 0.72$, $Re_D = 10$; (*g*) stationary, $Re_D = 50$; (*h*) perfect slip, $Re_D = 50$; (*i*) $\alpha_1 = 1.26$, $Re_D = 50$; (*j*) stationary, $Re_D = 300$; (*k*) perfect slip, $Re_D = 300$; (*l*) $\alpha_1 = 1.72$, $Re_D = 300$.

In the previous section we observed that the primary effect of the tangential surface velocity is to reduce the magnitude of vorticity generated at the cylinder surface. A relationship between vorticity and the power loss coefficient would aid in understanding of the Re_D dependence of the power loss coefficient. Using the relationship $\boldsymbol{\tau} : \nabla \boldsymbol{u} = \mu(|\boldsymbol{\omega}|^2 + \nabla \cdot (\boldsymbol{u} \cdot \nabla \boldsymbol{u}))$ net viscous dissipation can be expressed in terms of the net vorticity of the flow field and tangential surface velocity as (Lamb 1932; Stone & Samuel 1996):

$$\mu \int_0^{2\pi} \int_a^{\infty} \Phi_v r \, \mathrm{d}r \, \mathrm{d}\theta = 2\mu \int_0^{2\pi} u_\theta^2(a, \theta) \, \mathrm{d}\theta + \mu \int_0^{2\pi} \int_a^{\infty} \omega_z^2(r, \theta) r \, \mathrm{d}r \, \mathrm{d}\theta. \tag{4.2}$$

The extent to which the power loss coefficient can be minimized clearly depends on the relative contribution of the two terms in the right-hand side of (4.2) which are in competition with each other. The increase in C_{PL} due to a finite tangential surface velocity must be compensated for by a decrease in the contribution from vorticity for this to be a useful drag-reducing strategy.

Visualizations of the vorticity field depicted in figure 10 show the effect of Re_D on flow characteristics for perfect slip and the optimal flow configuration. The flow field corresponding to a stationary boundary is also included for comparison. When $Re_D \sim 1$ vorticity scales as U_∞/a so that contributions to the loss coefficient from both the tangential surface velocity and vorticity are of the same order of magnitude. Thus, a decrease in contribution from vorticity due to a prescribed finite tangential surface

https://doi.org/10.1017/jfm.2012.537 Published online by Cambridge University Press

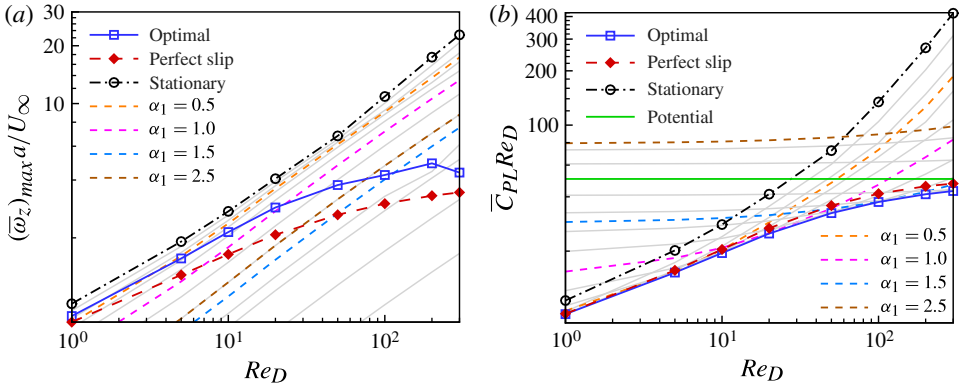


FIGURE 11. (Colour online) Maximum vorticity on the cylinder surface (a) and net power consumption (b) as a function of Re_D. Thin solid grey lines depict maximum vorticity and net power consumption for various α_1 ranging from 0.2 to 2.4 with increments of 0.2.

velocity is accompanied by a same order of magnitude increase in the contribution from the tangential surface velocity itself. Therefore, the reduction in the dissipation function achieved by the optimal configuration is not drastic when compared with the stationary case and even less when compared with the flow with a perfect slip boundary. As Re_D increases the contribution from vorticity begins to dominate and the reduction in energy loss for the optimal configuration becomes significant when compared with the stationary case. At even higher values of Re_D differences between the two become increasingly apparent and the advantage of the optimal configuration over the perfect slip is also discernible.

Figure 11(a) shows the maximum vorticity on the surface of the cylinder as a function of Re_D for the optimal configuration. The corresponding values for the stationary and perfect slip boundaries are also depicted in the figure and match well with those reported in Legendre *et al.* (2009). Thin solid grey lines show maximum vorticity as a function of Re_D for different α_1. In all of the cases, except potential flow when $\alpha_1 = 2$, maximum vorticity on the cylinder surface grows as $\sqrt{Re_D}$ in accordance with the predictions from boundary layer theory. This goes someway to explaining why a tangential surface velocity of the form investigated in this paper is successful in reducing the net power consumption especially at high Re_D. At high Re_D contribution from vorticity is the primary source of net dissipation (or power consumption) in the flow field so that an $O(1)$ increase in tangential surface velocity decreases dissipation by $O(Re)$ through a reduction in vorticity while generating a counter-productive increase of only $O(1)$. Therefore, the optimal tangential surface velocity leads to an increasingly energetically efficient drag reduction with rising Re_D. We also note that the maximum non-dimensional vorticity at the cylinder surface for the optimal configuration is less than 5 for all $Re_D \leqslant 300$, so that the adverse effects of separation on the net dissipation or power consumption are suppressed.

Figure 11(b) depicts the net dissipation in the flow field ($2\overline{P}_T/(\mu U_\infty^2) = \overline{C}_{PL} Re_D$) for stationary, perfect slip and optimal configuration as a function of Re_D. Thin solid grey lines in figure 11(b) depict net power consumption as a function of Re_D for constant α_1 in $u_w^t = -\alpha_1 U_\infty \sin\theta$. A finite α_1 suppresses boundary layer growth over the cylinder surface. Therefore, for a given α_1 the net power consumption first increases gradually with Re_D before eventually attaining a higher rate of increase that

https://doi.org/10.1017/jfm.2012.537 Published online by Cambridge University Press

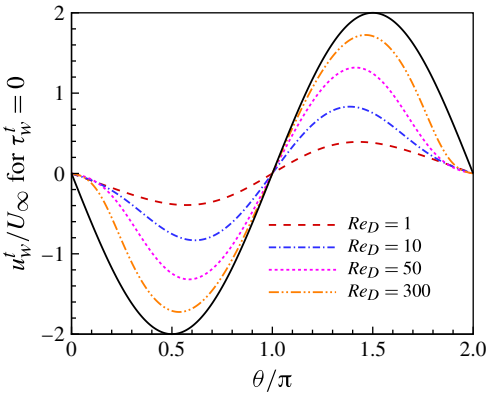


FIGURE 12. (Colour online) Tangential surface velocity for the flow with a perfect slip boundary for various Reynolds numbers. The solid line depicts the tangential surface velocity for the potential flow ($u_w^t = -2U_\infty \sin\theta$).

is consistent with prediction from boundary layer theory. The lower envelope of all of the curves corresponding to constant α_1 (depicted by a solid blue curve in the online version of figure 11*b*) gives the variation of power consumption for the optimal flow configuration.

Our results indicate that a tangential surface velocity corresponding to the potential flow which renders the flow field irrotational is very likely to lead to optimal power loss minimizing drag reduction as $Re_D \to \infty$. Further evidence for this statement comes from the fact that our numerical simulations at $Re_D = 1000$ (not reported here) lead to $\alpha_1^{opt} = 1.91$. In the limit $Re_D \to \infty$ it is hypothesized (Leal 1989) that vorticity for a perfect slip boundary will be confined to a very thin region surrounding the cylinder surface and the flow field will reduce to potential flow. Figure 12 depicts the tangential surface velocity profiles which lead to a vanishing shear stress corresponding to a perfect slip cylinder boundary. At the lowest $Re_D = 1$ the profile primarily involves only the first reflectionally symmetric mode ($\sin\theta$). As Re_D increases higher modes are required to ensure that the tangential wall shear stress vanishes. It is interesting to note that even for the moderate Reynolds numbers considered in this investigation the velocity profiles are tending towards the tangential surface velocity for a potential flow. This leads us to postulate that the tangential surface velocity corresponding to a perfect slip boundary, which led to optimal drag reduction for $Re_D \to 0$, will minimize power loss coefficient at sufficiently high Reynolds number also.

It would be useful to test the aforementioned postulate for $Re_D \to \infty$ through a theoretical analysis of the boundary layer equations for flow past a circular cylinder with a finite prescribed tangential surface velocity. A straightforward route to achieving this objective would involve solution of boundary layer equations for flow past a circular cylinder through the general Blasius series. Proceeding along the directions outlined in Schlichting (1960) one can show that the solution involves a series of ordinary differential equations, all linear, except the first one corresponding to a two-dimensional stagnation flow. Since each of the subsequent solutions depend on the preceding ones it is necessary to solve the ordinary differential equations in succession, starting from the first, while accounting for the wall motion through the boundary condition on the tangential surface velocity. The nonlinearity of the first

https://doi.org/10.1017/jfm.2012.537 Published online by Cambridge University Press

ordinary differential equation corresponding to flow at a plane stagnation point makes the problem analytically intractable even for the simple case of a stationary cylinder boundary. Therefore, even a first-order approximation to the solution of boundary layer equations, with a prescribed finite tangential surface velocity, can only be determined numerically. As a consequence a general expression relating net power consumption to a given tangential velocity profile cannot be derived and it is not possible to establish that the tangential surface velocity corresponding to potential flow is optimal for $Re_D \to \infty$.

An alternative, less general, but simpler way of proving the optimality of potential flow in minimizing power consumption for $Re_D \to \infty$ would involve consideration of boundary layer equations on a circular cylinder for small departures from potential flow. In such a case vorticity generated on the cylinder surface is only $O(1)$ (as opposed to $O(Re_D)$ for a stationary cylinder surface) so that boundary layer equations can be linearized following the analysis carried out in Moore (1963) for flow past a spherical bubble. For axisymmetric flow past a sphere of a radius a with perfect slip boundary we have the following result for total power consumption:

$$P_T = \int \Phi_v \, \mathrm{d}V = 12\pi\mu U_\infty^2 a \left\{ 1 - \frac{2.2}{\sqrt{Re_D}} + O(Re_D^{-1}) \right\}. \tag{4.3}$$

In the present context, one might consider flow past a circular cylinder for small departures from potential flow in the form of either a perfect slip boundary or a prescribed tangential surface velocity which involves only the first reflectionally symmetric mode ($u_w^t = -\alpha \sin\theta$, $|\alpha - 2| \ll 1$). We expect that the subsequent analysis based on linearization of boundary layer equations will bear close similarity with the one for flow past a spherical bubble and that the net dissipation rate will assume a similar form: $\int \Phi_v \, \mathrm{d}A = \int \Phi_v^{pot} \, \mathrm{d}A\{1 - C/\sqrt{Re_D} + O(Re_D^{-1})\}$, where Φ_v^{pot} denotes the dissipation function associated with the potential flow and C is a positive constant. The precise value of constant C can only be determined through a full consideration of not only the boundary layer but also the wake and the turning region at the stagnation point. Thus, in effect through this analysis we can only hope to show that a dissipation rate lower than that for potential flow is achievable for small departures from the tangential velocity corresponding to the potential flow, and that this reduction in the dissipation rate diminishes asymptotically as $Re_D \to \infty$. Since this key conclusion was emphasized in § 4.1.2 and was clearly evident in the simulation results presented in figures 8(*b*) and 11(*b*) we have not carried out a detailed linearized boundary layer analysis in this work.

For intermediate Reynolds numbers ($Re_D \gg 1$, $Re_D \ll \infty$) we have shown that optimal tangential surface velocities of the form $u_w^t = -\alpha_1^{opt} U_\infty \sin\theta$ reduce drag for a power loss coefficient that is lower than those for perfect slip and potential flow. Our search for a tangential surface velocity with a power loss coefficient which is lower than the optimal one reported in this paper was not successful. In particular, accounting for a finite slip length through Navier boundary condition only led to an increase in power loss coefficient beyond the value for a perfect slip boundary. A variation in the strength of the tangential surface velocity, while keeping the variation with θ the same as that for a perfect slip boundary, too did not yield any favourable results. However, despite the fact that introduction of higher modes always resulted in an increase in power loss coefficient, no conclusive statement can be made about whether or not the minimum power loss coefficients reported in this work represent a global minimum.

https://doi.org/10.1017/jfm.2012.537 Published online by Cambridge University Press

From the perspective of self-propulsion, as expected potential flow with $\alpha_1 = 2$ always resulted in zero drag and a power loss coefficient of $16\pi/Re_D$ at all Reynolds numbers considered in this investigation.

4.1.3. *Three-dimensional flow at* $Re_D = 300$

The results reported in the previous section were obtained from simulations which were restricted to a spanwise uniform flow past a two-dimensional circular cylinder. It is well known that the flow past a stationary circular cylinder with stationary boundaries becomes three-dimensional for $Re_D > 190$ (Williamson 1996). Therefore, it is important to analyse how the conclusions drawn previously are altered when three-dimensional effects are accounted for.

We conduct numerical simulations for flow past an infinitely long three-dimensional circular cylinder. The spanwise z direction is assumed to be periodic with a period of $L_z = 2\pi D$ and is discretized using a Fourier spectral collocation method. The numerical methodology adopted here is a straightforward extension of that utilized for the two-dimensional simulations. We consider flow at $Re_D = 300$; the maximum Reynolds investigated in two dimensions in the previous section. The computational domain extends out to $25D$ and is discretized using $300 \times 256 \times 64$ nodes in the r, θ and z directions, respectively. A time step of 5×10^{-3} is used for temporal discretization. A three-dimensional extension of the transient two-dimensional flow field, obtained from long time simulation of flow past a two-dimensional circular cylinder with a stationary boundary, is used as initial condition. The azimuthal component of the tangential surface velocity is kept at zero ($u_\theta(a, \theta, z, t) = 0$) for $t < 200D/U_\infty$ corresponding to a stationary cylinder boundary, except for a short time span of $5D/U_\infty$, at the beginning of the computations, when a small three-dimensional rotation is imparted in order to promote three-dimensional instabilities, with the purpose of reducing computational time. Thereafter, once the three-dimensional vortex shedding is established, the azimuthal component of the tangential surface velocity is ramped up gradually over the next $10D/U_\infty$ to $u_\theta = -1.72U_\infty \sin\theta$ corresponding to the power loss minimizing optimal tangential surface velocity profile obtained from two-dimensional computations in § 4.1.2. Thus, $u_\theta(a, \theta, z, t) = -1.72U_\infty \sin\theta$ for $t > 210D/U_\infty$. The primary objective here is to evaluate the susceptibility of the optimal configuration, determined through two-dimensional simulations in the previous section, to three-dimensional perturbations.

The evolution of the flow field is depicted in figure 13. The wake vortices are visualized using the isosurface of the λ_2 criterion (Jeong & Hussain 1995) coloured by ω_z, the component of vorticity in the z direction. The two-dimensional initial condition used for the simulation is shown in figure 13(*a*). As time progresses three-dimensional effects reduce the strength of the vortices in the wake of the cylinder (figure 13*b*). This results in a reduction in the drag and lift coefficients from a base value corresponding to the two-dimensional flow (figure 14). Between non-dimensional times of 200 and 210 the boundary condition is changed from stationary to that corresponding to two-dimensional optimal solution. As shown in figure 13(*c,d*), vorticity production at the cylinder surface diminishes and the three-dimensional vortical structures in the wake are convected away. At long times the drag and lift coefficients return back to values of 0.1 and 0, corresponding to the two-dimensional flow with optimal tangential surface velocity.

Thus, the flow with a spanwise constant optimal tangential surface velocity remains two-dimensional and steady at $Re_D = 300$. Since the two-dimensional optimal flow configuration is unaffected by the presence of three-dimensional perturbations for

https://doi.org/10.1017/jfm.2012.537 Published online by Cambridge University Press

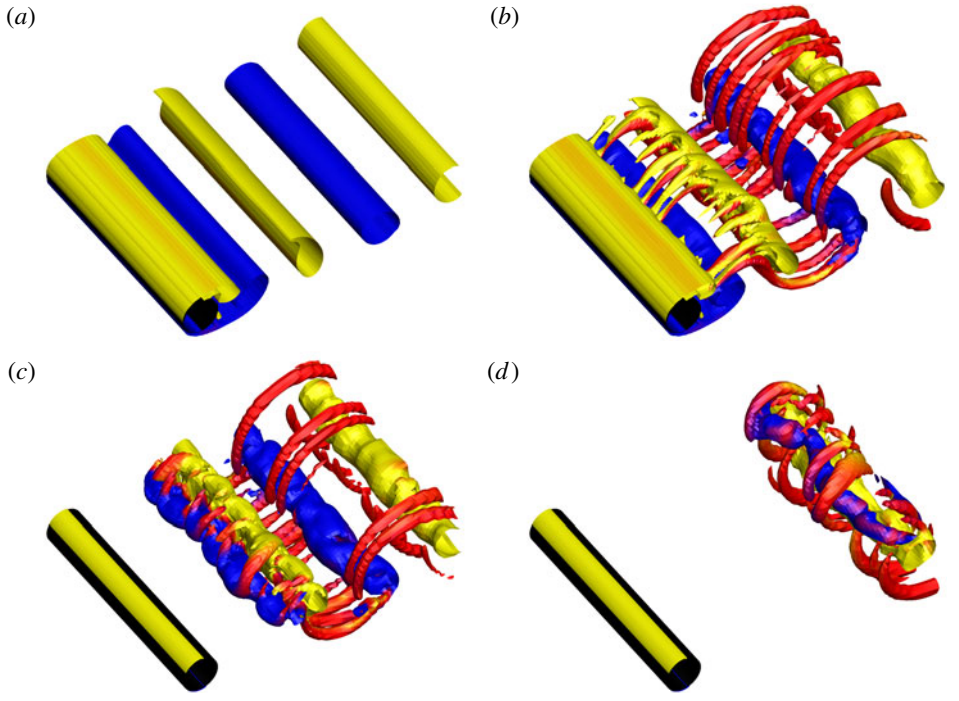


FIGURE 13. (Colour online) Vortical structures in the wake of the cylinder identified by $\lambda_2 = -0.2$: (*a*) $t = 0$; (*b*) $t = 200D/U_\infty$; (*c*) $t = 210D/U_\infty$; (*d*) $t = 220D/U_\infty$.

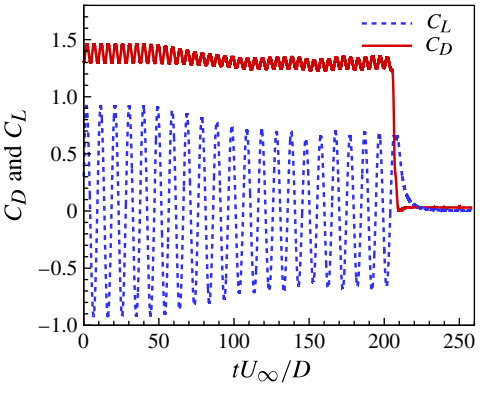


FIGURE 14. (Colour online) Drag and lift coefficients per unit length as a function of time for three-dimensional flow past a circular cylinder at $Re_D = 300$.

the highest Reynolds number investigated in this work we expect optimal flow configurations at remaining Re_D to follow a similar trend. A complete knowledge of the critical Reynolds number beyond which three-dimensional effects become significant for the optimal flow configurations will involve Floquet analysis such as that presented by Barkley & Henderson (1996). At present we may conclude that the optimal two-dimensional flow configurations obtained in this study are not susceptible to three-dimensional instabilities and the tangential velocities of the form $u_w^t = -\alpha_1^{opt} U_\infty \sin\theta$ will reduce drag while minimizing power loss coefficient in three dimensions also.

https://doi.org/10.1017/jfm.2012.537 Published online by Cambridge University Press

5. Drag reduction using piecewise constant tangential surface velocity

The tangential surface velocity profiles of the form $u_w^t = -U_\infty \alpha_1 \sin\theta$ were shown to be very useful from the perspective of energy loss minimization and drag reduction in the previous section. However, a velocity profile which varies sinusoidally along the cylinder periphery may not be convenient for practical implementation. What can be most easily realized in an experiment is to have several tangential belt actuators each moving with a constant surface velocity.

In this section we investigate whether or not a constant tangential surface velocity profile can be used to efficiently reduce drag acting on the cylinder. As discussed previously, related studies (Choi & Choi 2000; Milano & Koumoutsakos 2002) have investigated the effects of a prescribed piecewise constant tangential surface velocity on drag reduction without considering the energetic efficiency. In their three-dimensional study on flow past a cylinder, Poncet *et al.* (2008) prescribed the kinetic energy of the three-dimensional tangential surface velocity ($\int_S (u_w^t)^2/2\,\mathrm{d}A$) and sought its optimal distribution for drag reduction. Kinetic energy of the tangential surface velocity however represents only a fraction of the net power consumption (first term on the right-hand side of (4.2)) and the total energy loss (or power loss coefficient) associated with the optimal solution obtained in Poncet *et al.* (2008) is unknown.

Before considering the Reynolds number dependence via numerical simulations we conduct an analytical analysis of the problem for low Re_D using the techniques presented previously in § 3. For simplicity consider a two-dimensional problem similar to that formulated in § 3 with the following boundary condition for the tangential surface velocity:

$$f(\theta) = \frac{u_\theta(a,\theta)}{U_\infty} = \begin{cases} -a_1 & \text{if } 0 < \theta < \pi \\ a_1 & \text{if } \pi < \theta < 2\pi. \end{cases} \tag{5.1}$$

For convenience the tangential surface velocity given by (5.1) can be expressed in a Fourier series as follows:

$$f(\theta) = -\frac{4a_1}{\pi} \sum_{n=0}^{\infty} \frac{\sin((2n+1)\theta)}{2n+1}. \tag{5.2}$$

Using these values we obtain the following for drag and power loss coefficients:

$$C_D = \frac{8}{Re_D} \left\{ \frac{\pi - 2a_1}{\frac{1}{2} - \gamma - \ln(Re_D/8)} \right\}, \tag{5.3}$$

$$C_{PL} = \frac{4}{\pi Re_D} \left\{ \frac{(1 - \gamma - \ln(Re_D/8))16a_1^2 - 8\pi a_1 + 2\pi^2}{\frac{1}{2} - \gamma - \ln(Re_D/8)} + 16a_1^2 \sum_{n=1}^{\infty} \frac{1}{2n+1} \right\}. \tag{5.4}$$

Linear and quadratic dependence of the drag and power loss coefficients on a_1, a measure of the relative strength of the tangential surface velocity with respect to the free stream velocity, is confirmed from these expressions. It is also observed that the summation in the last term of (5.4) involves a divergent series for $a_1 \neq 0$ so that the power loss coefficient is infinite. This observation is linked to the singularity in tangential wall shear stress τ_w^t caused by a finite jump in u_w^t when $\theta = 0$ or π. The

https://doi.org/10.1017/jfm.2012.537 Published online by Cambridge University Press

product of τ_w^t and u_w^t is therefore no longer square integrable so that $\dot{W}$ and C_{PL} become unbounded.

While the aforementioned discussion is pertinent to the case of $Re_D \ll 1$ for a constant tangential surface velocity on each of the two halves of the cylinder, it is possible to show that the general conclusion on unboundedness of power loss coefficient will hold for arbitrary Re_D whenever a discontinuity in the tangential surface velocity (piecewise constant segments, for example) is encountered. Note that numerical simulations which attempt to approximate a discontinuity in the boundary condition for tangential surface velocity are also prone to this apparent ill-posedness in the calculation of $\dot{W}$ and an attempt at computing power loss coefficient leads to numerical values which continue to increase with mesh refinement even though a converged value for the drag coefficient is obtained. Since the power loss coefficient or an equivalent quantity was not reported in the study of Milano & Koumoutsakos (2002), it is not possible to assess the effect of discontinuous piecewise constant tangential velocities on the net power consumption. In their later studies, Poncet *et al.* (2008) focused on optimization of spanwise variations in tangential surface velocity and chose a three-dimensional extension of the two-dimensional smooth base profile obtained by fitting the piecewise continuous optimal two-dimensional tangential surface velocity profiles (Poncet & Koumoutsakos 2005). However, this choice was made to circumvent the problems associated with interactions of three-dimensional instabilities with a discontinuous tangential surface velocity and not because of its detrimental effect on net power consumption.

A similar situation is encountered in the widely studied lid-driven cavity flow problem where the singularity at the two upper corners of the moving boundary leads to a divergence of viscous stresses and total work done (Nie, Robbins & Chen 2006). A breakdown in the continuum-based description of the flow near the singular corners is the root cause behind the unphysical divergence of stresses. Fully atomistic and hybrid multiscale methods which couple continuum description of the flow field away from these corners to an atomistic description have been proposed to resolve this issue (Koplik & Banavar 1995; Qian & Wang 2005; Nie *et al.* 2006). A continuum description was found to be adequate for a physical description of the flow field provided that it was coupled with a Navier boundary condition which accounted for the presence of a finite slip near singular corners (Qian & Wang 2005). The slip length was estimated from a molecular dynamics simulation of fluid atoms confined between moving lower and upper solid walls. Solid walls were modelled using atoms constrained to fcc lattice sites (atoms positioned at the face centres and corners of a cubic unit cell) through a harmonic spring and their density was assumed to be about 2.3 times that of the fluid. Lennard–Jones potentials were used for interatomic interactions with the energy scale and range of interaction chosen to model fluid–fluid and solid–fluid interactions.

The task of coupling atomistic and continuum models within a single framework is a non-trivial one and although it has been accomplished for the driven cavity flow we are not aware of any such computation for flow past a cylinder with moving boundaries where the tangential surface velocity may be discontinuous. The absence of an estimate for the slip length, which in general could depend on Re_D and a_1, prevents us from using a continuum description with Navier boundary condition instead of the no-slip boundary condition. Furthermore, the validity of a continuum description with Navier boundary condition for flow past a circular cylinder is open to question and can only be established through a multiscale or atomistic simulation.

https://doi.org/10.1017/jfm.2012.537 Published online by Cambridge University Press

Given these facts we attempt to regularize the discontinuity in tangential surface velocity in a way that alleviates the problems associated with the estimation of the power loss coefficient. This objective can be achieved by ensuring the continuity of tangential surface velocity along the cylinder periphery so that the product $u_w^t \tau_w^t$ becomes square integrable. Therefore, we assume that a physically realistic approximation to the flow field corresponding to the original discontinuous boundary condition given by (5.1) can be obtained by replacing it with the following

$$u_\theta(a,\theta) = -a_1 U_\infty \quad \text{if } \theta_0 < \theta < \pi - \theta_0, \tag{5.5a}$$

$$u_\theta(a,\theta) = a_1 U_\infty \quad \text{if } \pi + \theta_0 < \theta < 2\pi - \theta_0, \tag{5.5b}$$

$$\tau_{r\theta}(a,\theta) = 0 \quad \text{if } 0 \leqslant \theta \leqslant \theta_0, \text{ or } \pi - \theta_0 \leqslant \theta \leqslant \pi + \theta_0, \text{ or } 2\pi - \theta_0 \leqslant \theta \leqslant 2\pi, \tag{5.5c}$$

where θ_0 gives the portion of the boundary on which a regularization is applied through a perfect slip boundary condition. Thus, the parameter θ_0 represents the non-dimensional length scale over which the transition from a slip to a no-slip boundary occurs.

There are obvious limitations of this approach. The parameter θ_0 is an unknown and its relationship with a physical length scale is not immediately clear. One possibility is to view it as a length scale over which continuum-based models no longer provide a reliable approximation of the flow field and an atomic description is necessary. Even though the boundary condition given by (5.5) ensures continuity of the tangential surface velocity, tangential stress remains unphysical in the sense that it is unbounded at the locations where the boundary condition changes from a prescribed tangential velocity to a prescribed tangential stress. Note however that this does not lead to an unbounded power loss coefficient and we can still hope to investigate how effective the use of piecewise constant tangential surface velocity is in reducing drag and power loss coefficients.

We consider numerical solution of the incompressible Navier–Stokes equations in two dimensions with the boundary conditions given by (2.2*a*) and (5.5) using the second-order projection method described in § 4. A singularity subtraction technique is employed and the governing equations are reposed in terms of perturbed variables in order to circumvent problems related to slow convergence which are anticipated when high-order methods are used for computing solutions that are not sufficiently smooth. Details of the singular solution and the modified governing equations in terms of perturbed variables along with the numerical methodology are given in appendix A.

A series of simulations are performed to assess the effect of the strength of the tangential surface velocity a_1 on drag and power loss coefficients at a fixed $Re_D = 100$. A computational grid, similar to that utilized previously, with 300×256 $(N_r \times N_\theta)$ nodes is used with a time step size of 2×10^{-3}. The value of the parameter θ_0 is set equal to 5.6^0 and a total of 16 computational nodes out of 256 in the θ direction are used for the approximation of the perfect slip boundary condition in (5.5). Figure 15(*a*) depicts the tangential surface velocity profile which approximates the tangential wall boundary condition given by (5.5). The drag and power loss coefficients are depicted in figure 15(*b*). The overall trends are similar to those observed in figure 6(*a*) in the previous section for variation of only the first reflectionally symmetric mode corresponding to α_1. Power loss coefficient attains a minimum value of 0.677 when $a_1 = 0.8$ corresponding to $C_D = 0.582$. The cylinder achieves a state of self-propulsion corresponding to $C_D = 0$ when $a_1 \approx 1.54$. It is interesting to note that the first Fourier mode corresponding to a piecewise constant tangential surface velocity given by (5.1) with $a_1 \approx 1.54$ is not very different from 2. Therefore, the first Fourier mode of a

https://doi.org/10.1017/jfm.2012.537 Published online by Cambridge University Press

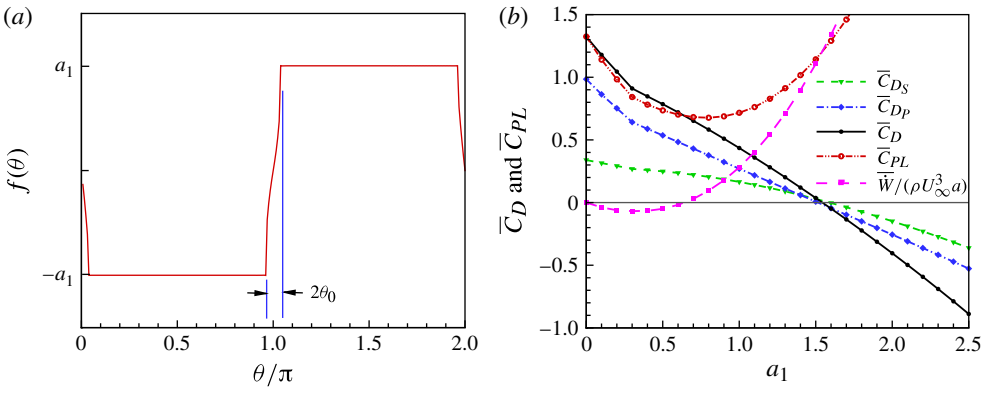


FIGURE 15. (Colour online) (*a*) Computed tangential surface velocity for the boundary condition given by (5.5) with two piecewise constant segments over the cylinder surface at $Re_D = 100$. (*b*) Drag and power loss coefficients as a function of the strength of the tangential surface velocity with respect to the free stream at $Re_D = 100$.

piecewise constant tangential surface velocity given by (5.5), which ensures that the drag acting on the circular cylinder vanishes, is the same as that for a potential flow ($\alpha_1 = 2$ for potential flow). Thus, the first mode has a primary influence on the drag coefficient and the presence of higher modes in the piecewise constant tangential surface velocity given by (5.5) implies that a self-propelled state is achieved for a $C_{PL} \approx 1.21$ which is much higher than a value of 0.503 for the potential flow.

The minimum power loss coefficient obtained by varying the strength of a tangential surface velocity which is constant on each of the two halves of the circular cylinder turned out to be significantly higher than the one that could be obtained by retaining only the first mode with a finite α_1 and $\alpha_n = 0$ for $n > 1$. This drawback could be alleviated, at least to some extent, by introducing additional segments of piecewise constant tangential velocities through an increase in the number of tangential belt controllers along the cylinder periphery. In order to demonstrate this we consider a configuration in which the tangential belt actuators are distributed on the surface of the circular cylinder in a manner which approximates a sine wave profile using six piecewise constant segments. As before a small region with perfect slip is utilized to circumvent the problems associated with convergence of power loss coefficient in the presence of a finite jump in the tangential surface velocity. The boundary condition for the tangential surface velocity now reads

$$u_\theta(a,\theta) = -a_3 U_\infty \quad \text{if } \frac{\pi}{4} + \theta_0 < \theta < \frac{3\pi}{4} - \theta_0, \tag{5.6a}$$

$$u_\theta(a,\theta) = -a_3 \frac{\sqrt{2-\sqrt{2}}}{2} U_\infty \quad \text{if } \theta_0 < \theta < \frac{\pi}{4} - \theta_0 \text{ or } \frac{3\pi}{4} + \theta_0 < \theta < \pi - \theta_0, \tag{5.6b}$$

$$u_\theta(a,\theta) = \left.\begin{array}{l} a_3 \dfrac{\sqrt{2-\sqrt{2}}}{2} U_\infty \quad \text{if } \pi + \theta_0 < \theta < \dfrac{5\pi}{4} - \theta_0 \text{ or} \\ \dfrac{7\pi}{4} + \theta_0 < \theta < 2\pi - \theta_0 \end{array}\right\}, \tag{5.6c}$$

https://doi.org/10.1017/jfm.2012.537 Published online by Cambridge University Press

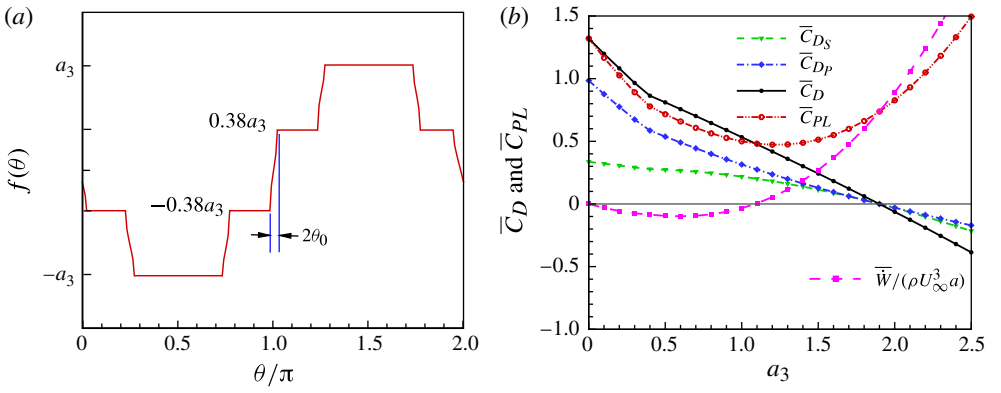


FIGURE 16. (Colour online) (*a*) Computed tangential surface velocity for the boundary condition given by (5.6) with six piecewise constant segments over the cylinder surface at $Re_D = 100$. (*b*) Drag and power loss coefficients as a function of the strength of the tangential surface velocity with respect to the free stream at $Re_D = 100$.

$$u_\theta(a,\theta) = a_3 U_\infty \quad \text{if } \frac{5\pi}{4} + \theta_0 < \theta < \frac{7\pi}{4} - \theta_0, \tag{5.6d}$$

$$\tau_{r\theta}(a,\theta) = 0 \quad \text{otherwise.} \tag{5.6e}$$

We consider the same set of simulation runs except with a modified boundary condition given by (5.6). Figure 16(*a*) depicts the velocity profile with six equally spaced piecewise constant steps approximating a sinusoidal profile. The drag and power loss coefficients obtained from the simulations are shown in figure 16(*b*) as a function of the strength of the tangential surface velocity relative to the free stream. A minimum C_{PL} of 0.473 is achieved when $a_3 \approx 1.2$ corresponding to a drag coefficient of 0.418. Clearly increasing the number of piecewise constant segments from one to three on each side of the cylinder results in a substantial improvement. Furthermore, the drag on the cylinder vanishes when $a_3 \approx 1.9$. The first Fourier mode attains a value of 1.96 for the tangential profile given by (5.6) with $a_3 = 1.9$ and $\theta_0 = 0$. This is consistent with our previous findings in that the drag coefficient is influenced primarily by a change in the first mode. Although still higher than the potential flow ($C_{PL}^{pot} = 0.503$ at $Re_D = 100$), the power loss coefficient of 0.737 associated with this self-propelling configuration is significantly lower than that given above for two segments of piecewise constant tangential surface velocity. In principle further systematic reductions in the power loss coefficient could be achieved by appropriately increasing the number and varying the length of segments with piecewise constant tangential surface velocity used to approximate the sine profile.

6. Conclusions

In summary, a general analysis of the energy budget for flow past a two-dimensional circular cylinder with moving boundaries has been presented and a relationship between the net power consumption and the rate at which work must be done against the drag force and the tangential stresses which resist the motion of the cylinder boundary has been established. The drawbacks of using relative drag reduction or power savings ratio as a performance metric for the current investigation were highlighted. Therefore, a non-dimensional power loss coefficient, defined in (2.8),

https://doi.org/10.1017/jfm.2012.537 Published online by Cambridge University Press

was used to quantify the energetic efficiency in the general cases of drag reduction, thrust generation and self-propulsion, corresponding to positive, negative and zero drag coefficients, respectively. The power loss coefficient is related to the total viscous dissipation in the flow field. At high Reynolds numbers, the power loss coefficient can be usefully thought to represent the rate at which kinetic energy is left behind in the wake.

At low Re_D, Oseen equations for flow past a two-dimensional circular cylinder placed in a uniform free stream were solved for any prescribed time-independent reflectionally symmetric tangential surface velocity. Explicit expressions for the velocity and pressure fields were derived along with the drag force and net power consumption. A tangential surface velocity which resulted in perfect slip boundary condition with vanishing tangential shear stress along the cylinder surface was found to reduce drag and minimize the net power consumption. Only the first mode led to a reduction in drag and higher modes led to an increase in power consumption without influencing drag when $Re_D \ll 1$ ((3.18) and (3.17)).

Numerical simulations were used to investigate the effect of a prescribed tangential surface velocity with only the first mode ($u_w^t = -\alpha_1 U_\infty \sin\theta$) on the drag and power loss coefficients at various Reynolds numbers ranging from 1 to 300. At a Reynolds number of 100, a gradual increase in the strength of the tangential surface velocity (α_1) led to suppression of vortex shedding, detachment of the standing eddy that is formed behind the cylinder and its subsequent disappearance. At each Reynolds number an optimal strength (α_1^{opt}) corresponding to a minimum in power loss coefficient was identified. The minimum power loss coefficients achieved through this optimal strength were found to be lower than those for a perfect slip boundary and potential flow at all Reynolds numbers. The maximum vorticity at the cylinder surface, corresponding to the optimal strengths, remained $O(1)$ so that the vorticity accumulation in the wake was insufficient for boundary layer separation and the formation of a recirculating region.

A break up of the net power consumption into contributions from vorticity and the tangential surface velocity through (4.2) allowed a closer inspection into the Reynolds number dependence of the power loss coefficient. A decrease in vorticity contribution is offset by an increase in contribution from the tangential surface velocity and a balance between the two leads to minimum power loss coefficient. At high Reynolds numbers, the contribution from vorticity dominates and the potential flow solution is likely to give the minimum power loss coefficient for $Re_D \to \infty$. The two-dimensional flow fields corresponding to minimum power loss coefficients were insensitive to three-dimensional perturbations and introduction of a spanwise uniform two-dimensional tangential surface velocity of the form $u_w^t = -\alpha_1^{opt} U_\infty \sin\theta$ was found to suppress spanwise vortical structures which are formed behind an impulsively started circular cylinder at a Reynolds number of 300.

The utility of tangential belt actuators in reducing drag and power loss coefficients was demonstrated through a careful choice of the strengths of segments with piecewise constant tangential surface velocities. Conclusions derived previously under the strict assumption of $Re_D \ll 1$ seem to extend to finite Reynolds numbers in that the drag coefficient was influenced only by the first mode of the tangential surface velocity and the remaining higher modes led to an increase in power loss coefficient. Results from numerical simulations at $Re_D = 100$, with one and three segments of constant tangential surface velocity on each of the two halves of the circular cylinder, led us to argue that a self-propelling state achieved through a tangential surface velocity

https://doi.org/10.1017/jfm.2012.537 Published online by Cambridge University Press

corresponding to the potential flow is likely to minimize the power loss coefficient at all Reynolds numbers.

For convenience the main results of the present investigation have been summarized in table 1. Results from related studies which control the flow past a circular cylinder and achieve drag reduction through tangential surface motion have also been included for comparison. An especially attractive feature of the results obtained in the present study is the high energetic efficiency which is reflected in the remarkably low drag and power loss coefficients. While these results do not guarantee a global minimum in the net power consumption the minimum power loss coefficients, and the corresponding drag coefficients, are significantly lower than those reported previously. The proposed way of decreasing drag has an additional advantage of reducing the dissipation and vorticity in the wake which could be beneficial for noise reduction in self-propelling bodies.

Several aspects of the current investigation deserve further attention. The effect of higher modes in the tangential surface velocity, at finite Re_D, on the power loss coefficient needs to be ascertained through more rigorous analysis and refined simulations. The possibility of achieving power loss coefficients which are lower than the minimum reported in this study, through three-dimensional or time-varying tangential surface velocities, cannot be ruled out. The bulk of the simulations were conducted for relatively low Reynolds numbers ($\leqslant 300$) and it is unclear whether or not the general conclusions will be applicable at high Reynolds numbers especially when flow becomes turbulent. Related drag-reduction strategies such as those based on transverse wall oscillations (Karniadakis & Choi 2003) or blowing and suction (Kim & Choi 2005; Dong, Triantafyllou & Karniadakis 2008) are also worth exploring. This investigation focused on a simple two-dimensional bluff body flow. It would be useful to investigate the form of the optimal tangential surface velocity which leads to energetically efficient drag reduction and propulsion for more complex bluff bodies. For a body of arbitrary shape (4.2) takes the following general form

$$\mu \int_V \Phi_v \, \mathrm{d}V = 2\mu \int_\Gamma (u_w^t)^2 \, \kappa \, \mathrm{d}s + \mu \int_V \boldsymbol{\omega} \cdot \boldsymbol{\omega} \, \mathrm{d}V, \tag{6.1}$$

where κ denotes the curvature of a curve which lies on the boundary of the bluff body. One can speculate that a tangential surface velocity corresponding to potential flow would be optimal for streamlined bodies when their largest dimension is aligned with the direction of the flow. This would also imply that potential flow will be least effective for drag reduction and propulsion of a body whose largest dimension is orthogonal to the flow direction. Our future work involves further analysis of the aforementioned issues.

Acknowledgements

Support provided by Indian Space Research Organization-Indian Institute of Science Space Technology Cell and Naval Research Board is gratefully acknowledged.

Appendix A. Singularity subtraction technique

In this section we outline the details of the singularity subtraction technique used for the numerical solution of the two-dimensional incompressible Navier–Stokes equations (2.1) along with the boundary conditions given by (2.2*a*) and (5.5). The second boundary condition on the tangential surface velocity and wall shear stress is of the

https://doi.org/10.1017/jfm.2012.537 Published online by Cambridge University Press

mixed kind so that the stress and pressure are expected to be singular at points $\theta = \theta_0$, $\pi - \theta_0$, $\pi + \theta_0$ and $2\pi - \theta_0$. The velocity on the other hand remains continuous.

An attempt to directly solve the discrete system of equations, which results from a numerical approximation of the aforementioned problem, is expected to lead to a loss of accuracy related to the poor convergence of high-order methods when applied to singular problems. It is therefore recommended that the most singular part in the solution be removed analytically before a numerical approximation is sought. Following previous works (Botella & Peyret 1998; Auteri, Parolini & Quartapelle 2002) the singular solution to the problem at hand can be expressed in an asymptotic series of the following form:

$$\boldsymbol{u}^S = \boldsymbol{u}_0^S + Re_D \boldsymbol{u}_1^S + Re_D^2 \boldsymbol{u}_2^S + \cdots \tag{A 1}$$

$$p^S = \frac{1}{Re_D} p_0^S + p_1^S + Re_D p_2^S + \cdots \tag{A 2}$$

where the singular solutions $\boldsymbol{u}^S$ and p^S satisfy

$$\boldsymbol{u}^S \cdot \boldsymbol{\nabla} \boldsymbol{u}^S = -\frac{1}{\rho} \boldsymbol{\nabla} p^S + \nu \nabla^2 \boldsymbol{u}^S, \quad \boldsymbol{\nabla} \cdot \boldsymbol{u}^S = 0, \tag{A 3}$$

and the following boundary conditions

$$u_r^S(a, \theta) = 0 \tag{A 4}$$

$$u_\theta^S(a, \theta) = \begin{cases} -a_1 U_\infty & \text{if } \theta_0 < \theta < \pi - \theta_0 \\ a_1 U_\infty & \text{if } \pi + \theta_0 < \theta < 2\pi - \theta_0 \\ a \left. \dfrac{\partial u_\theta^S}{\partial r} \right|_{r=a} & \text{otherwise.} \end{cases} \tag{A 5}$$

In order to keep the analysis simple we retain only the leading term in the singular contribution so that $\boldsymbol{u}^S = \boldsymbol{u}_0^S$ and $p^S = p_0^S / Re_D$ and Oseen equations can be used to determine the analytical form assumed by the singular solution. This singular solution is then subtracted from the original governing equations to obtain a more regular problem in terms of the perturbed variables $(\tilde{\boldsymbol{u}}, \tilde{p})$:

$$\frac{\partial \tilde{\boldsymbol{u}}}{\partial t} + \boldsymbol{N}(\tilde{\boldsymbol{u}}) = -\frac{1}{\rho} \boldsymbol{\nabla} \tilde{p} + \nu \nabla^2 \tilde{\boldsymbol{u}} + \tilde{\boldsymbol{f}}^S, \quad \boldsymbol{\nabla} \cdot \tilde{\boldsymbol{u}} = 0, \tag{A 6}$$

$$\boldsymbol{N}(\tilde{\boldsymbol{u}}) = \tilde{\boldsymbol{u}} \cdot \boldsymbol{\nabla} \tilde{\boldsymbol{u}} + \boldsymbol{u}_{\boldsymbol{0}}^S \cdot \boldsymbol{\nabla} \tilde{\boldsymbol{u}} + \tilde{\boldsymbol{u}} \cdot \boldsymbol{\nabla} \boldsymbol{u}_{\boldsymbol{0}}^S \tag{A 7}$$

$$\tilde{\boldsymbol{f}}^S = -\frac{1}{\rho Re_D} \boldsymbol{\nabla} p_0^S + \nu \nabla^2 \boldsymbol{u}_{\boldsymbol{0}}^S - \boldsymbol{u}_{\boldsymbol{0}}^S \cdot \boldsymbol{\nabla} \boldsymbol{u}_{\boldsymbol{0}}^S \tag{A 8}$$

with

$$\tilde{u}_r(a, \theta) = 0 \tag{A 9}$$

$$\tilde{u}_\theta(a, \theta) = \begin{cases} 0 & \text{if } \theta_0 < \theta < \pi - \theta_0 \text{ or } \pi + \theta_0 < \theta < 2\pi - \theta_0 \\ a \left. \dfrac{\partial \tilde{u}_\theta}{\partial r} \right|_{r=a} & \text{otherwise.} \end{cases} \tag{A 10}$$

where $\tilde{\boldsymbol{u}} = \boldsymbol{u} - \boldsymbol{u}_{\boldsymbol{0}}^S$ and $\tilde{p} = p - p_0^S / Re_D$.

https://doi.org/10.1017/jfm.2012.537 Published online by Cambridge University Press

A.1. *Singular solution*

In order to determine the leading terms $(\boldsymbol{u}_{\boldsymbol{0}}^S, p_0^S)$ in the singular solution we compare (A 5) with the expressions for the tangential surface velocity and tangential shear stress given by (2.14) and (3.13*b*), respectively, to obtain the following dual series for the Fourier coefficients α_i^S

$$\sum_{n=0}^{\infty} \alpha_{2n+1}^S \sin(2n+1)\theta = a_1 \quad \text{if } \theta_0 < \theta < \pi/2 \tag{A 11}$$

$$\sum_{n=0}^{\infty} (2n+1)\alpha_{2n+1}^S \sin(2n+1)\theta = \beta(2-\alpha_1^S)\sin\theta \quad \text{if } 0 \leqslant \theta < \theta_0 \tag{A 12}$$

where only the odd coefficients have been retained ($\alpha_{2n}^S = 0$ for $n = 1, 2, \ldots$) since $\boldsymbol{u}_{\boldsymbol{0}}^S$ is reflectionally symmetric and $\beta = 1/(1 - 2\gamma - 2\ln(ka/2))$. Following the general procedure described in Sneddon (1966) we obtain the following for the Fourier coefficients

$$\alpha_{2n+1}^S = \beta\left(2-\alpha_1^S\right)\left\{\frac{P_{2n}(\cos\theta_0) - P_{2n+2}(\cos\theta_0)}{4n+3} - \frac{P_{2n-1}(\cos\theta_0) - P_{2n+1}(\cos\theta_0)}{4n+1}\right\} + \frac{2a_1}{\pi}\left\{\frac{P_{2n}(\cos\theta_0) + P_{2n+1}(\cos\theta_0)}{2n+1}\right\}, \quad n = 1, 2, 3, \ldots \tag{A 13}$$

where

$$\alpha_1^S = \frac{4\beta\sin^4\left(\dfrac{\theta_0}{2}\right) + \dfrac{4a_1}{\pi}\cos^2\left(\dfrac{\theta_0}{2}\right)}{1 + 2\beta\sin^4\left(\dfrac{\theta_0}{2}\right)}. \tag{A 14}$$

The velocity and pressure fields can be expressed in terms of these coefficients as follows:

$$u_{0r}^S(r,\theta) = U_\infty\cos\theta\left[\left(1-\frac{a^2}{r^2}\right) + \left\{(1-\gamma)\left(1-\frac{a^2}{r^2}\right) + \frac{a^2}{r^2}\ln\left(\frac{ka}{2}\right) - \ln\left(\frac{kr}{2}\right)\right\} \times (2-\alpha_1^S)\beta\right] + \sum_{n=1}^{\infty}\frac{U_\infty(2n+1)\alpha_{2n+1}^S}{2} \times \left\{\left(\frac{a}{r}\right)^{2n} - \left(\frac{a}{r}\right)^{2n+2}\right\}\cos(2n+1)\theta \tag{A 15}$$

$$u_{0\theta}^S(r,\theta) = -U_\infty\sin\theta\left[\left(1+\frac{a^2}{r^2}\right) + \left\{(1-\gamma)\left(1+\frac{a^2}{r^2}\right) - \frac{a^2}{r^2}\ln\left(\frac{ka}{2}\right) - \ln\left(\frac{kr}{2}\right) - 1\right\}(2-\alpha_1^S)\beta\right] + \sum_{n=1}^{\infty}\frac{U_\infty\alpha_{2n+1}^S}{2}\left\{(2n-1)\left(\frac{a}{r}\right)^{2n} - (2n+1)\left(\frac{a}{r}\right)^{2n+2}\right\}\sin(2n+1)\theta \tag{A 16}$$

$$p_0^S(r,\theta) = p_\infty - \frac{1}{2}\rho U_\infty^2\left\{\left(\frac{a}{r}\right)^4 - \left(\frac{a}{r}\right)^2\cos 2\theta\right\} - \frac{2\mu U_\infty(2-\alpha_1^S)\beta}{r} + \frac{4\mu U_\infty}{a}\sum_{n=1}^{\infty} n\alpha_{2n+1}^S\left(\frac{a}{r}\right)^{2n+1}\cos(2n+1)\theta. \tag{A 17}$$

https://doi.org/10.1017/jfm.2012.537 Published online by Cambridge University Press

A singular solution obtained by retaining the first 1000 terms in the above series has been used to compute results presented in § 5.

A.2. *Numerical methodology*

Governing equations (A 6), (A 7) and (A 8) and boundary conditions given by (A 9) and (A 10) are discretized with the second-order semi-implicit projection method of Hugues & Randriamampianina (1998). As depicted in figure 3, the boundary conditions for the velocity field change from Dirichlet to Robin to Neumann along the outer boundary of the computational domain. Since the boundary conditions on velocity field are no longer of the same kind (Dirichlet, Neumann or Robin) for all $\theta \in [0, 2\pi]$, standard fast-Fourier-transform-based techniques cannot be applied in their original form in order to compute a numerical solution. Here we have used an influence matrix technique (Kleiser & Schumann 1980) which exploits the linearity of the Helmholtz equations for the velocity fields to determine appropriate values on the boundary which would yield a desired Neumann or Robin boundary condition. Thus, only Helmholtz equations need to be solved at each step of the computation and the influence matrix and its LU decomposition can be conveniently computed and stored at the beginning of the calculations (Peyret 2001).

The flows that are of interest in this current work involve generation and subsequent convection of large vortical structures in the wake behind the circular cylinder. It is necessary to ensure that the boundary condition prescribed on the outflow boundary does not lead to spurious oscillations that typically result from the interaction of wake vortices with the exit boundary. The boundary condition at the outflow boundary (see figure 3) ensures that the normal derivative of the velocity is equal to that corresponding to the potential flow. The normal (radial) derivatives of the velocity field corresponding to a potential flow scale as $\partial_r \boldsymbol{u}^{pot} \sim (a/r)^3$ so that $\partial_r \boldsymbol{u}^{pot} \to 0$ for $r \gg a$. Therefore, the outflow boundary condition chosen in the current work closely corresponds to a homogeneous Neumann boundary condition and is significantly different than a Dirichlet boundary condition which would prescribe the velocity to be the same as that for a potential flow. As we shall see below this choice suppresses spurious reflections when compared with a purely Dirichlet boundary condition all along the outflow boundary ($\boldsymbol{u} = \boldsymbol{u}^{pot}$) and allows the large-scale vortical structures to exit the computational domain without significant distortions.

We consider a test case chosen specifically to assess the effectiveness of the outflow boundary conditions. Following Mittal & Balachandar (1996) we consider generation and subsequent advection of an isolated pair of vortices and monitor their evolution as they exit from the computational domain. The initial conditions for this test case correspond to flow past an impulsively started circular cylinder with stationary boundary conditions at $Re_D = 300$, the highest Reynolds number considered in this work. Once a vortex pair is formed in the wake of the circular cylinder, the boundary conditions for the tangential velocity on the surface of the circular cylinder are changed to those corresponding to a potential flow ($u_w^t = -2U_\infty \sin\theta$ for $t \geqslant 10$). This stops vorticity production at the cylinder surface so that the isolated vortex pair formed initially when $t < 10$ convects downstream continuously before leaving the computational domain.

We consider two test runs on a computational domain which extends out to $25.5a$, where a denotes the radius of the cylinder. All of the parameters are kept the same in the two simulations except that we use the mixed boundary conditions described in § 2.2 and figure 3 of the revised manuscript for the first test run while the second involves use of a Dirichlet boundary condition on the entire outer

https://doi.org/10.1017/jfm.2012.537 Published online by Cambridge University Press

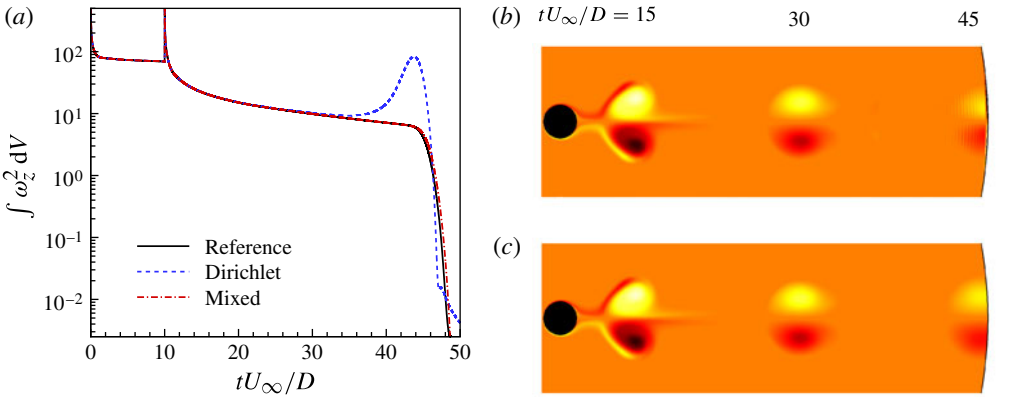


FIGURE 17. (Colour online) (*a*) Comparison of the total vorticity in the domain as a function of time for computations using Dirichlet and mixed boundary conditions. Vorticity isocontours for the outflow test case with (*b*) Dirichlet and (*c*) mixed boundary conditions in the outflow region. Reference solution is obtained from a simulation performed on an extended computational domain at a higher resolution.

boundary $\boldsymbol{u}(R_{out}, \theta) = \boldsymbol{u}^{pot}(R_{out}, \theta)$, $\theta \in [0, 2\pi)$, where $R_{out} = 25.5a$ denotes the outer radius of the computational domain. Results from these simulations are compared with a reference solution that is obtained through a similar test run which involves use of a mixed outflow boundary condition on a computational which extends out to $R_{out} = 50a$. A comparison of the two test runs with the reference solution computed on the extended domain should allow us to assess the appropriateness of the outflow boundary condition in capturing wake behind the circular cylinder.

Figure 17(*a*) depicts a comparison of the evolution of the total vorticity in a computational domain with $R_{out} = 25.5a(\int_a^{25.5a} \omega_z^2 r \, dr \, d\theta)$, computed using the two methods, with the reference solution. The numerical solution obtained using the Dirichlet boundary condition begins to show deviations from the reference solution for $t \gtrapprox 35$ due to spurious reflections that occur once the vortices start interacting with the outflow boundary condition. In contrast, the solution computed using the mixed outflow boundary condition preserves the total vorticity in the computational domain throughout the simulation. The spurious reflections at the outflow boundary for the solution computed using the Dirichlet boundary condition are also evidenced in the vorticity isocontours depicted in figure 17(*b*) at $t = 45$. As shown in figure 17(*c*) the solution computed using mixed boundary condition remains free of these numerical artefacts.

A similar methodology of discretization using high-order compact schemes for solving Navier–Stokes equations in vorticity-streamfunction formulation was presented and extensively validated in a previous work (Shukla, Tatineni & Zhong 2007). The principal differences between the current implementation and that in Shukla *et al.* (2007) include the use of a fast and exponentially accurate Fourier spectral method for discretization in the θ direction and a primitive variable formulation which extends naturally to three dimensions. Extensive tests were carried out for the purpose of validation of the current numerical code. A brief summary is presented in table 2. It is observed that the computed results are in good agreement with those reported in previous studies for a cylinder with a stationary and a perfect slip boundary at various Re_D.

https://doi.org/10.1017/jfm.2012.537 Published online by Cambridge University Press

https://doi.org/10.1017/jfm.2012.537 Published online by Cambridge University Press

Boundary	Reference	$Re_D = 5$	$Re_D = 20$	$Re_D = 100$			$Re_D = 200$		
		C_D	C_D	$\overline{C}_D$	C_L^{max}	St	$\overline{C}_D$	C_L^{max}	St
Stationary	Present	4.036	2.069	1.344	0.330	0.166	1.341	0.680	0.197
	Legendre *et al.* (2009)	4.065	2.035	1.350	0.334	0.176	1.345	0.70	0.204
	Dennis & Chang (1970)	4.116	2.045	—	—	—	—	—	—
	Chan *et al.* (2011)	—	—	1.338	0.325	0.164	1.340	0.68	0.196
	Liu, Zheng & Sung (1998)	—	—	1.350	0.339	0.165	1.31	0.69	0.192
	Poncet (2004)	—	—	—	—	—	1.339	0.70	0.199
	Henderson (1994)	—	—	—	—	0.165	—	—	0.197
	Williamson (1996) (Experiments)	—	—	—	—	0.164	—	—	0.197
	Chan *et al.* (2011) (Experiments)	—	—	—	—	0.163	—	—	0.197
		C_D	C_D		C_D			C_D	
Perfect slip	Present	3.130	1.340		0.417			0.229	
	Legendre *et al.* (2009)	3.15	1.33		0.415			0.228	

TABLE 2. Drag and lift coefficients and Strouhal number (St) as a function of Re_D from two-dimensional computations.

REFERENCES

ABRAMOWITZ, M. & STEGUN, I. 1968 *Handbook of Mathematical Functions*. Dover.

ARAKERI, J. H. & SHUKLA, R. K. 2012 A unified view of energetic efficiency in active drag reduction, thrust generation and self-propulsion through a loss coefficient with some applications. *J. Fluid Struct.* (submitted).

AUTERI, F., PAROLINI, N. & QUARTAPELLE, L. 2002 Numerical investigation on the stability of singular driven cavity flow. *J. Comput. Phys.* **183**, 1–25.

BARKLEY, D. & HENDERSON, R. D. 1996 Three-dimensional floquet stability analysis of the wake of a circular cylinder. *J. Fluid Mech.* **322**, 215–241.

BATCHELOR, G. K. 1967 *An Introduction to Fluid Dynamics*. Cambridge University Press.

BEAUDOIN, J.-F., CADOT, O., AIDER, J.-L. & WESFREID, J.-E. 2006 Drag reduction of a bluff body using adaptive control methods. *Phys. Fluids* **18**, 085107.

BECHERT, D. W., HAGE, W. & BRUSEK, M. 1996 Drag reduction with the slip wall. *AIAA J.* **34** (5), 1072–1074.

BERGMANN, M. & CORDIER, L. 2008 Optimal control of the cylinder wake in the laminar regime by trust-region methods and POD reduced-order models. *J. Comput. Phys.* **227**, 7813–7840.

BERGMANN, M., CORDIER, L. & BRANCHER, J.-P. 2005 Optimal rotary control of the cylinder wake using proper orthogonal decomposition reduced-order model. *Phys. Fluids* **17**, 097101.

BERGMANN, M., CORDIER, L. & BRANCHER, J.-P. 2006 On the generation of a reverse von Karman street for the controlled cylinder wake in the laminar regime. *Phys. Fluids* **18**, 028101.

BLACKBURN, H. M., ELSTON, J. R. & SHERIDAN, J. 1999 Bluff-body propulsion produced by combined rotary and translational oscillation. *Phys. Fluids* **11**, 4–6.

BLANCO, A. & MAGNAUDET, J. 1995 The structure of the axisymmetric high-Reynolds number flow around an ellipsoidal bubble of fixed shape. *Phys. Fluids* **7**, 1265–1274.

BOTELLA, O. & PEYRET, R. 1998 Benchmark spectral results on the lid-driven cavity flow. *Comput. Fluids* **27**, 421–433.

CHAN, A. S., DEWEY, P. A., JAMESON, A., LIANG, C. & SMITS, A. J. 2011 Vortex suppression and drag reduction in the wake of counter-rotating cylinders. *J. Fluid Mech.* **679**, 343–382.

CHOI, B. & CHOI, H. 2000 Drag reduction with a sliding wall in flow over a circular cylinder. *AIAA J.* **38** (4), 715–717.

CHOI, S., CHOI, H. & KANG, S. 2002 Characteristics of flow over a rotationally oscillating cylinder at low Reynolds number. *Phys. Fluids* **14**, 2767–2777.

CHOI, H., JEON, W.-P. & KIM, J. 2008 Control of flow over a bluff body. *Annu. Rev. Fluid Mech.* **40**, 113–139.

DENNIS, S. C. R. & CHANG, G.-Z. 1970 Numerical solutions for steady flow past a circular cylinder at Reynolds numbers up to 100. *J. Fluid Mech.* **42**, 471–489.

DONG, S., TRIANTAFYLLOU, G. S. & KARNIADAKIS, G. E. 2008 Elimination of vortex streets in bluff-body flows. *Phys. Rev. Lett.* **100**, 204501.

HAPPEL, J. & BRENNER, H. 1965 *Low Reynolds Number Hydrodynamics*. Prentice-Hall.

HE, J.-W., GLOWINSKI, R., METCALFE, R., NORDLANDER, A. & PERIAUX, J. 2000 Active control and drag optimization for flow past a circular cylinder. I. Oscillatory cylinder rotation. *J. Comput. Phys.* **163**, 83–117.

HENDERSON, R. D. 1994 Unstructured spectral element methods: parallel algorithms and simulations. PhD thesis, Princeton University.

HOMESCU, C., NAVON, I. M. & LI, Z. 2002 Suppression of vortex shedding for flow around a circular cylinder using optimal control. *Intl J. Numer. Meth. Fluids* **38**, 43–69.

HUGUES, S. & RANDRIAMAMPIANINA, A. 1998 An improved projection scheme applied to pseudospectral methods for the incompressible Navier–Stokes equations. *Intl J Numer. Meth. Fluids* **28**, 501–521.

JEON, S. & CHOI, H. 2005 Suboptimal feedback control for drag reduction in flow over a sphere. *Bull. Am. Phys. Soc*.

JEONG, J. & HUSSAIN, F. 1995 On the identification of a vortex. *J. Fluid Mech.* **285**, 69–94.

JOSEPH, D. D., FUNADA, T. & WANG, J. 2007 *Potential Flows of Viscous and Viscoelastic Fluids*. Cambridge University Press.

https://doi.org/10.1017/jfm.2012.537 Published online by Cambridge University Press

KARNIADAKIS, G. E. & CHOI, K.-S. 2003 Mechanisms on transverse motions in turbulent wall flows. *Annu. Rev. Fluid Mech.* **35**, 45–62.

KIM, J. & CHOI, H. 2005 Distributed forcing of flow over a circular cylinder. *Phys. Fluids* **17**, 033103.

KLEISER, L. & SCHUMANN, U. 1980 Treatment of incompressibility and boundary conditions in 3-D numerical spectral simulations of plane channel flows. *Proceedings, 3rd GAMM Conference on Numerical Methods in Fluid Mechanics*, pp. 165–169.

KOPLIK, J. & BANAVAR, J. R. 1995 Corner flow in the sliding plate problem. *Phys. Fluids* **7**, 3118–3125.

KUMAR, S., GONZALEZ, B. & PROBST, O. 2011 Flow past two rotating cylinders. *Phys. Fluids* **23**, 014102.

LAMB, H. 1932 *Hydrodynamics*. Cambridge University Press.

LAUGA, E. & POWERS, T. R. 2009 The hydrodynamics of swimming microorganisms. *Rep. Prog. Phys.* **72**, 096601.

LEAL, L. G. 1989 Vorticity transport and wake structure for bluff bodies at finite Reynolds number. *Phys. Fluids* **1**, 124–131.

LEGENDRE, D., LAUGA, E. & MAGNAUDET, J. 2009 Influence of slip on the dynamics of two-dimensional wakes. *J. Fluid Mech.* **633**, 437–447.

LESCHZINER, M. A., CHOI, H. & CHOI, K.-S. 2011 Flow-control approaches to drag reduction in aerodynamics: progress and prospects. *Phil. Trans. R. Soc.* A **369**, 1349–1351.

LESHANSKY, A. M., KENNETH, O., GAT, O. & AVRON, J. E. 2007 A frictionless microswimmer. *New J. Phys. Fluids* **9**, 145.

LIGHTHILL, M. J. 1952 On the squirming motion of nearly spherical deformable bodies through liquids at very small Reynolds numbers. *Commun. Pure Appl. Maths* **5**, 109–118.

LIU, C., ZHENG, X. & SUNG, C. H. 1998 Preconditioned multigrid methods for unsteady incompressible flows. *J. Comput. Phys.* **139**, 35–57.

MAGNAUDET, J. & EAMES, I. 2000 The motion of high-Reynolds-number bubbles in inhomogeneous flows. *Annu. Rev. Fluid Mech.* **32**, 659–708.

MILANO, M. & KOUMOUTSAKOS, P. 2002 A clustering genetic algorithm for cylinder drag optimization. *J. Comput. Phys.* **175**, 79–107.

MITTAL, R. & BALACHANDAR, S. 1996 Direct numerical simulation of flow past elliptic cylinders. *J. Comput. Phys.* **124**, 351–367.

MITTAL, S. & KUMAR, B. 2003 Flow past a rotating cylinder. *J. Fluid Mech.* **476**, 303–334.

MODI, V. J. 1997 Moving surface boundary-layer control: a review. *J. Fluid. Struct.* **11**, 627–663.

MOORE, D. W. 1963 The boundary layer on a spherical gas bubble. *J. Fluid Mech.* **16**, 161–176.

MURALIDHAR, P., FERRER, N., DANIELLO, R. & ROTHSTEIN, J. P. 2011 Influence of slip on the flow past superhydrophobic circular cylinders. *J. Fluid Mech.* **680**, 459–476.

NAZARINIA, M., JACONO, D. L., THOMPSON, M. C. & SHERIDAN, J. 2009 The three-dimensional wake of a cylinder undergoing a combination of translational and rotational oscillation in a quiescent fluid. *Phys. Fluids* **21**, 064101.

NIE, X., ROBBINS, M. O. & CHEN, S. 2006 Resolving singular forces in cavity flow: multiscale modelling from atomic to millimetre scales. *Phys. Rev. Lett.* **96**, 134501.

PEYRET, R. 2001 *Spectral Methods for Incompressible Viscous Flow*. Springer.

PONCET, P. 2004 Topological aspects of three-dimensional wakes behind rotary oscillating cylinders. *J. Fluid Mech.* **517**, 27–53.

PONCET, P., HILDEBRAND, R., COTTET, G.-H. & KOUMOUTSAKOS, P. 2008 Spatially distributed control for optimal drag reduction of the flow past a circular cylinder. *J. Fluid Mech.* **599**, 111–120.

PONCET, P. & KOUMOUTSAKOS, P. 2005 Optimization of vortex shedding in 3-D wakes using belt actuators. *Intl J. Offshore Polar Engng* **15**, 1–7.

PRANDTL, L. & TIETJENS, O. G. 1957 *Applied Hydro- and Aerodynamics*. Dover.

PROTAS, B. & STYCZEK, A. 2002 Optimal rotary control of the cylinder wake in the laminar regime. *Phys. Fluids* **14**, 2073–2087.

PURCELL, E. M. 1977 Life at low Reynolds number. *Am. J. Phys.* **45**, 3–11.

QIAN, T. & WANG, X.-P. 2005 Driven cavity flow: from molecular dynamics to continuum hydrodynamics. *SIAM Multiscale Model. Simul.* **3**, 749–763.

https://doi.org/10.1017/jfm.2012.537 Published online by Cambridge University Press

ROTHSTEIN, J. P. 2010 Slip on superhydrophobic surfaces. *Annu. Rev. Fluid Mech.* **42**, 89–109.

SCHLICHTING, H. 1960 *Boundary Layer Theory*. McGraw-Hill.

SHIELS, D. & LEONARD, A. 2001 Investigation of a drag reduction on a circular cylinder in rotary oscillation. *J. Fluid Mech.* **431**, 297–322.

SHUKLA, R. K., TATINENI, M. & ZHONG, X. 2007 Very high-order compact finite difference schemes on non-uniform grids for incompressible Navier–Stokes equations. *J. Comput. Phys.* **224**, 1064–1094.

SHUKLA, R. K. & ZHONG, X. 2005 Derivation of high-order compact finite difference schemes for non-uniform grid using polynomial interpolation. *J. Comput. Phys.* **204**, 404–429.

SNEDDON, I. N. 1966 *Mixed boundary value problems in potential theory*. John Wiley & Sons.

SPALART, P. R. & MCLEAN, J. D. 2011 Drag reduction: enticing turbulence, and then an industry. *Phil. Trans. R. Soc.* A **369**, 1556–1569.

STONE, H. A. & SAMUEL, A. D. T. 1996 Propulsion of microorganisms by surface distortions. *Phys. Rev. Lett.* **77**, 4102–4104.

TAYLOR, G. I. 1952 The action of waving cylindrical tails in propelling microscopic organisms. *Proc. R. Soc.* A **211**, 225–239.

THIRIA, B., GOUJON-DURAND, S. & WESFREID, J. E. 2006 The wake of a cylinder performing rotary oscillations. *J. Fluid Mech.* **560**, 123–147.

TOKUMARU, P. T. & DIMOTAKIS, P. E. 1991 Rotary oscillation control of a cylinder wake. *J. Fluid Mech.* **224**, 77–90.

TOMOTIKA, S. & AOI, T. 1950 The steady flow of viscous fluid past a sphere and circular cylinder at small Reynolds numbers. *Q. J. Mech. Appl. Maths* **3**, 140–161.

VEYSEY, J. & GOLDENFELD, N. 2007 Simple viscous flows: from boundary layers to the renormalization group. *Rev. Mod. Phys.* **79**, 883–927.

WILLIAMSON, C. H. K. 1996 Vortex dynamics in the cylinder wake. *Annu. Rev. Fluid Mech.* **28**, 477–539.

YOON, H. S., KIM, J. H., CHUN, H. H. & CHOI, H. J. 2007 Laminar flow past two rotating circular cylinders in a side-by-side arrangement. *Phys. Fluids* **19**, 128103.

YOU, D. & MOIN, P. 2007 Effects of hydrophobic surfaces on the drag and lift of a circular cylinder. *Phys. Fluids* **19**, 081701.

https://doi.org/10.1017/jfm.2012.537 Published online by Cambridge University Press